Oxygen saturation surrounding deep-water formation events in the Labrador Sea from Argo-O_2 data

by

Mitchell Wolf
B.Sc., University of Victoria, 2013

A Thesis Submitted in Partial Fulfillment
of the Requirements for the Degree of

MASTER OF SCIENCE

in the School of Earth and Ocean Sciences

Supervisory Committee

Oxygen saturation surrounding deep-water formation events in the Labrador Sea from Argo-O_2 data

by

Mitchell Wolf
B.Sc., University of Victoria, 2013

Supervisory Committee

Roberta Hamme (School of Earth and Ocean Sciences)
Supervisor

Jody Klymak (School of Earth and Ocean Sciences)
Departmental Member

Denis Gilbert (Fisheries and Oceans Canada, Maurice Lamontagne Institute)
Additional Member

Abstract

Deep-water formation supplies oxygen-rich water to the deep sea, spreading throughout the ocean via the global thermohaline circulation. Models suggest that gases in newly formed deep-water do not come to equilibrium with the atmosphere. However, direct measurements during wintertime convection are scarce, and the controls over the extent of this disequilibria are poorly quantified. Here we show that oxygen is consistently undersaturated at -6.3% to -7.6% in the Labrador Sea at the end of convection, when convection reaches deeper than 800 m. Deeper convection resulted in greater undersaturation while convection lasting later in the year resulted in values closer to equilibrium, from which we produce a predictive relationship. We use dissolved oxygen data from six profiling Argo floats in the Labrador Sea between 2003 to 2016, allowing direct observations of wintertime convection. Four of the six optode oxygen sensors displayed *in situ* drift of -2.98 μmol O_2 kg^{-1} $year^{-1}$ on average, which we corrected to stable deep-water oxygen values from repeat hydrography. Observations of low oxygen intrusions during restratification and a simple mixing calculation demonstrate that lateral processes act to lower the oxygen inventory of the central Labrador Sea. This suggests that the Labrador Sea is a net sink for atmospheric oxygen, but uncertainties in parameterizing gas exchange limit our ability to quantify the net uptake. Our results constrain the initial oxygen concentration of Labrador Sea Water and allow more precise estimates of oxygen utilization and nutrient regeneration in this water mass.

Table of Contents

List of Tables

List of Figures

Acknowledgments

This project would not have been possible without the support of many people. I would first like to thank my supervisor Roberta Hamme for her countless hours of help and dedication to this work. I would also like to thank my committee members, Denis Gilbert and Jody Klymak, and Igor Yashayaev for their valuable input throughout this thesis.

I would also like to thank funding from NSERC through the VITALS network. Argo data were collected and made freely available by the International Argo Program and the national programs that contribute to it. (http://www.argo.ucsd.edu, http://argo.jcommops.org). The Argo Program is part of the Global Ocean Observing System. http://doi.org/10.17882/42182#48844. CCMP Version-2.0 vector wind analyses are produced by Remote Sensing Systems. Data are available at www.remss.com. NCEP Reanalysis data provided by the NOAA/OAR/ESRL PSD, Boulder, Colorado, USA, from their Web site at http://www.esrl.noaa.gov/psd/.

Dedication

This thesis is dedicated to my family. My parents, Leslie and Peter, whose help and encouragement never wavered. To my grandparents, Nana, Papa, and Omi, for endless support and for creating the miraculous family that has kept me afloat. To my brother Sam and sister Stephanie, for all the laughs and keeping me posted on family events while my head was buried in this work. To all my aunts and uncles who have shown wonderful interest in my work. A special thanks to Karen and Jim for dozens of dinners and home modifications while I was a starving, helpless student. To my girlfriend Steph for her infinite patience and understanding while I worked late into the night or went to sea. And finally to all my friends who never fail to entertain me over drinks or around the camp fire.

Key Points

- At end of convection, Labrador Sea mixed layer consistently -6.3% to -7.6% undersaturated in oxygen when convection was deeper than 800m

- Oxygen more undersaturated when convection is deeper or when convection ends earlier resulting in predictive relationship

- Lateral input of low oxygen waters during restratification provides evidence that the Labrador Sea is a region of net oxygen uptake

1. Introduction

Deep-water formation is important because it is the mechanism by which the deep ocean communicates with the atmosphere, facilitating exchanges of heat and important gases such as carbon dioxide and oxygen [*Lab Sea Group*, 1998; *Azetsu-Scott et al.*, 2003; *DeGrandpre et al.*, 2006]. The large wintertime heat loss in these regions drives ocean uptake of carbon dioxide and oxygen, while export of newly formed deep-water redistributes dissolved gases from the poles to low latitudes and influences global climate [*Lazier et al.*, 2002]. Our study focuses on the Labrador Sea, a key region for uptake of anthropogenic carbon [*Khatiwala et al.*, 2013], which slows the rise of atmospheric carbon dioxide [*Sabine et al.*, 2004; *Steinfeldt et al.*, 2009] but also increases ocean acidification [*Azetsu-Scott et al.*, 2010]. High-latitude warming in response to climate change may strengthen stratification in the Labrador Sea [*Böning et al.*, 2016; *Dickson et al.*, 2007a], reduce deep-water formation and the amount of carbon dioxide uptake, and decrease deep ocean oxygen as has been observed in intermediate waters around the world [*Gilbert,* 2017*; Gilbert et al.*, 2010; *Keeling et al.*, 2010]. Since there are no internal sources of oxygen below the euphotic zone, a weakening of deep-water formation would disrupt crucial deep-sea habitats and change the preservation of organic material in sediments through oxygen deprivation [*Cowie et al.*, 1995].

In this study, we determine the oxygen content of newly-formed deep waters and quantify net oxygen uptake. Unlike most of the world's surface ocean where dissolved oxygen is close to equilibrium [*Najjar and Keeling*, 1997; *Broecker and Peng*, 1982],

deep convection regions do not fully equilibrate with the atmosphere [*Clark and Coote*, 1988]. Respiration within the water column utilizes oxygen, creating an oxygen deficit in deeper waters. This low oxygen water is mixed to the surface during convection. During deep-water formation in the Labrador Sea, the entrainment of low oxygen water into the mixed layer and subsequent mixing and sinking happens on a faster timescale than the counteracting air-sea gas exchange, so the undersaturated surface water sinks before it can fully equilibrate [*Körtzinger et al.*, 2008].

Quantifying the extent of surface oxygen disequilibria will improve studies using apparent oxygen utilization (AOU) to determine respiration and regenerated nutrients in the ocean interior [*Carlson et al.*, 2010; *Duteil et al.*, 2012, 2013]. AOU is meant to quantify how much oxygen has been consumed since the water was last at the surface and typically assumes that oxygen in the surface ocean is at equilibrium with the atmosphere everywhere. However, the majority of the ocean interior was last at surface at high-latitude deep-water formation sites, such as the Labrador Sea, during winter when surface waters are typically undersaturated with respect to oxygen. Model results show that AOU likely overestimates the amount of oxygen consumed by respiration by 10-30 μmol kg^{-1} in the deep North Atlantic, a large proportion of the <100 μmol kg^{-1} AOU signal observed in these waters [*Ito et al.*, 2004; *Duteil et al.*, 2013]. These model results need to be confirmed by direct observations of surface oxygen disequilibria, also known as preformed oxygen, during deep-water formation events, but such observations are scarce. The preformed oxygen values determined by our study will provide a correction to AOU

estimates in Labrador Sea Water, an important component of the North Atlantic Deep Water.

The Labrador Sea, our study site, is one of the most thoroughly studied regions of deep convection in the world [e.g. *Kieke and Yashayaev,* 2015 *and references within*]. This area is influenced by strong physical and biological forcings centered around the cyclonic subpolar gyre in the North Atlantic [*Lab Sea Group*, 1998]. The center of the Labrador Sea is characterized by doming isopycnals that are weakly stratified due to deep winter convection, forming Labrador Sea Water. Successive years of winter convection can precondition the water column for extremely deep convection by weakening stratification in the region [*Yashayaev and Loder*, 2017]. The winter mixing is fueled by cold, dry air coming from the Canadian continent and removing heat from the Labrador Sea [*Schulze et al.,* 2016]. In the first half of winter, the mixed layer remains shallow while cooling rapidly until the salinity stratification is overcome; then, progressively deepening convection dominates the second half of winter. This mixing resupplies the surface waters with nutrients, helping to fuel the large spring phytoplankton bloom. The complex interplay between atmospheric forcing and preconditioning resulting in Labrador Sea deep convection [*Yashayaev and Loder*, 2017] leads to strong interannual variability with convection depths ranging from less than 600 m to greater than 1700 m [*Yashayaev*, 2007; *Yashayaev and Loder*, 2016]. If the depth of convection controls how closely oxygen approaches equilibrium, varying deep-water formation events will create waters with varying oxygen concentrations.

We make use of autonomous sensors as an important resource for investigating deep convection, because only a handful of ship-based oxygen measurements have been made during the Labrador Sea's deep convection period due to rough seas [*Clark and Coote,* 1988; *Zimmerman et al.*, 2000]. Dissolved oxygen measurements in the ocean have significantly increased since the early 2000's due to profiling floats equipped with oxygen sensors [*Johnson et al.*, 2009], and are planned to increase still further with the Biogeochemical-Argo (BGC-Argo) Program [*Biogeochemical-Argo Planning Group*, 2016]. Over 800 Argo floats have been equipped with oxygen sensors [*doi:10.17882/42182#48844*]. Typically, these floats drift at 1000 m depth for 10 days, then sink to 2000 m before rising to the surface. As they ascend, they take *in situ* measurements of dissolved oxygen, salinity, and temperature at specific depths, then transmit this data when surfaced via satellite. This cycle is repeated every 10 days for the duration of the float's lifetime, typically 4 years. Dissolved oxygen profiles from Argo floats have been used to understand ocean-atmosphere processes such as air-sea gas exchange [*Kihm and Körtzinger,* 2010] and ocean ventilation / oxygen inventory gain during deep convection [*Körtzinger et al.*, 2004], biogeochemical processes such as carbon export [*Martz et al.*, 2008] and net community production [*Riser and Johnson,* 2008; *Plant et al.*, 2016], and the stability of oxygen minimum zones [*Prakash et al.*, 2012]. Complimentary to profiling floats, moorings equipped with oxygen sensors have also been used to study the oxygen inventory gain and air-sea flux during deep convection in the Labrador Sea [*Koelling et al.*, in prep.] and to describe the seasonal cycle of oxygen [*Körtzinger et al.*, 2008].

In this study, we use oxygen data from Argo-O_2 floats to investigate how competing oceanic processes occurring during deep convection affect how closely oxygen concentrations approach equilibrium by the end of convection. In addition, strong interannual variability of convection in the Labrador Sea [*Yashayaev et al.*, 2007; *Yashayaev and Loder*, 2016] motivates us to determine how the degree of equilibration varies from year to year, particularly with respect to the depth and end date of convection. In Section 2, we describe our methods including the details of each float used, data processing methods, and calculations of the oxygen inventory and air-sea fluxes. In Section 3, we describe our technique to calibrate oxygen optode sensors to stable deep-water oxygen values determined from repeat hydrography. In Section 4, we examine the seasonal cycle of oxygen and then the processes affecting the end of convection oxygen values, particularly depth and end date of convection, followed by investigating net oxygen uptake from a comparison of air-sea and lateral fluxes to the observed oxygen inventory.

2. Methods

2.1 Data Selection

We used dissolved oxygen data from 6 Argo floats [*Argo*, 2000; *doi:10.17882/42182#48844*] that were active in the Labrador Sea between 2003 and 2016 (Table 1), resulting in 15 individual observations of wintertime convection. We selected floats that spent multiple winters in the Labrador Sea, had regular profiles to 2000 m, and whose data were readily available online with sufficient information regarding data processing or a PI contact with whom processing could be verified. We excluded 6 other Canadian Argo floats equipped with oxygen optodes that spent time in the Labrador Sea, because three were confined to the boundary currents (4900879, 4900880, and 4901141) while the other three, despite spending some time in the central Labrador Sea, never observed winter convection (4901142, 4901780, and 4901782). All float oxygen data were calibrated as described in Section 3. We focused our study on the region in the Labrador Sea where deep convection is most likely to occur (black boundary in Figure 1). We based our study region on a combination of the observed regions of weak stratification and maximum buoyancy loss [*Lab Sea Group,* 1998] as well as loosely on the 2500 m isobath. Float profiles outside of this region were excluded from the analysis.

All oxygen data used in this study comes from Aanderaa optodes. The three newest floats use Aanderaa optode model 4330 while the older three floats use optode model 3830 (Table 1). Both models use dynamic quenching, measuring the phase shift in the fluoresced excitation signal occurring when oxygen interacts with the lumiphores

within the sensing foil. This phase shift is then used to calculate the oxygen concentration [*Tenberg et al.*, 2006]. The stability of these optodes is discussed in Section 3.

Table 1: Argo float information for all floats used in this study. IF indicates Ifremer, France, while ME indicates MEDS, Canada. Drift rates are the mean annual drift for an individual float's entire lifespan (see Section 3). The gain equations provide a time dependent function that can be multiplied by the float's oxygen saturation values (determined from Argo DOXY values corrected following Section 2.2) to obtain calibrated values, where δt is days since deployment. The root mean squared error (RMSE) between the fit function and the float measured oxygen saturation at 1800-1900 m is also given.

Float ID	Data Centre	PI Name	First Profile Date	Sensor Model	Drift Rate ($\mu mol\ kg^{-1}\ yr^{-1}$)	Drift Rate ($So_2\%\ yr^{-1}$)	Gain Equation $G(t) = So_2^{Deep} / F(t)$	RMSE of fit (So_2[%])
1901210	IF	Virginie Thierry	17-Aug-2011	Aanderaa Optode 4330	-2.93	-0.80	$85.84 / (-5.43 \cdot [1-\exp(-\delta t / 1.66 \times 10^3)] + 80.89)$	0.12
1901217	IF	Virginie Thierry	26-Jul-2011	Aanderaa Optode 4330	-3.21	-0.95	$85.84 / (-6.12 \cdot [1-\exp(-\delta t / 1.20 \times 10^3)] + 80.04)$	0.14
6901030	IF	Virginie Thierry	16-Jul-2012	Aanderaa Optode 4330	-4.27	-1.08	$85.84 / (-3.58 \cdot [1-\exp(-\delta t / 7.46 \times 10^2)] + 80.04)$	0.07
4900494	ME	Blair Greenan	4-Jun-2004	Aanderaa Optode 3830	-1.52	-0.35	$86.35 / (-9.50 \times 10^{-4} \cdot \delta t + 88.53)$	0.16
4900611	IF	Jens Schimanski	22-Sep-2004	Aanderaa Optode 3830	-0.20	-0.07	$86.35 / (-1.92 \times 10^{-4} \cdot \delta t + 79.34)$	0.12
4900607	IF	Jens Schimanski	14-Sep-2003	Aanderaa Optode 3830	-1.00	-0.43	$87.22 / (-1.20 \times 10^{-3} \cdot \delta t + 87.10)$	0.16

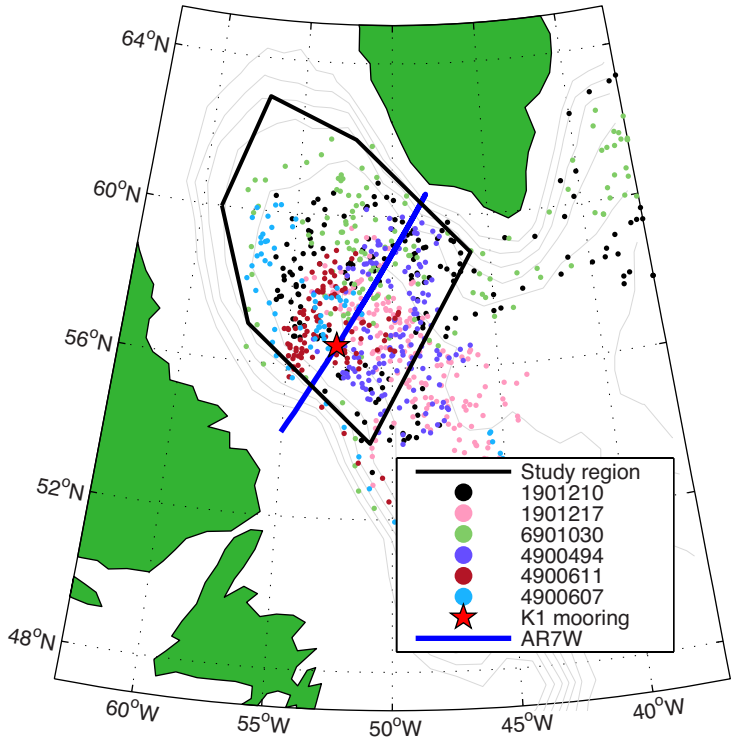

Figure 1. Locations of each individual float profile from all six floats used in this study with float numbers indicated in legend. The black line indicates the study region for our analysis. The red star indicates the K1 mooring location. The blue line indicates the AR7W hydrographic line. Grey lines indicate bathymetry at 500 m intervals, starting at 1000 m.

2.2 Pressure and Salinity Corrections

At the time of data acquisition, raw dissolved oxygen values from floats 1901210, 1901217, 6901030, and 4900494 were corrected for pressure [*Uchida et al.,* 2008] and salinity effects at the Argo National Data Centers according to the "Processing Argo OXYGEN data at the DAC level, Version 1.3" manual [*Thierry et al.,* 2013]. We updated the pressure correction to that recommended by *Bittig et al.* [2015] according to the "Processing Argo OXYGEN data at the DAC level, Version 2.2" manual [*Thierry et al.*, 2016]. This new pressure correction gives constant oxygen concentrations in deeply

convecting layers while the old correction showed average changes of 3.14 μmol kg^{-1} /1000 m (Appendix A). Floats 4900611 and 4900607 had no pressure or salinity corrections applied at the time of data acquisition. We applied the pressure correction recommended by *Bittig et al.* [2015] and salinity correction according to the newest processing manual [*Thierry et al.*, 2016], noting that floats 4900611 and 4900607 had internal reference salinities of 35 and zero respectively. Which version of the processing manual has been used by the DAC for most optode floats in the Argo database remains unclear; we recommend inquiring with the float PI when necessary.

2.3 Convection End Date

We needed to define the end of convection date to investigate the oxygen saturation anomaly at the end of convection (see Section 4.2). Choosing the end of convection date was done visually by inspecting individual profiles of temperature, salinity, potential density, and calibrated dissolved oxygen and oxygen saturation anomaly on a float-by-float and year-by-year basis (Appendix B). We chose the end of convection profile as the profile with the maximum mixed layer depth with subsequent profiles showing some sort of restratification in the surface waters or horizontal advection of waters outside the region penetrating the profiles mid-depth. We also considered convection duration as a metric. However, determining the start of convection date was more subjective, and our results were robust to the choice of end of convection date vs. convection duration (Appendix C).

2.4 Oxygen Saturation

We use both oxygen saturation and oxygen saturation anomaly in this paper. These expressions of the deviation of oxygen concentrations from equilibrium drive the air-sea flux of oxygen, controlling how much oxygen uptake or outgassing occurs. Oxygen saturation (So_2) is the ratio (as a percent) of measured oxygen concentration to the oxygen concentration of water at equilibrium with the atmosphere based on potential temperature and salinity, while the oxygen saturation anomaly (ΔO_2) is defined as the percent difference between the actual measured oxygen concentration and the oxygen concentration of water at equilibrium with the atmosphere.

$$So_2 = \left(\frac{\left[O_2\right]_{float}}{\left[O_2\right]_{eq}} \right) \bullet 100\% \quad , \qquad \Delta O_2 = \left(\frac{\left[O_2\right]_{float}}{\left[O_2\right]_{eq}} - 1 \right) \bullet 100\% \tag{1}$$

where $[O_2]_{float}$ is the oxygen concentration measured by the float and $[O_2]_{eq}$ is the oxygen concentration at equilibrium with the atmosphere calculated using *Garcia and Gordon* [1992, 1993] and float measured potential temperature and salinity.

2.5 Air-Sea Oxygen Flux

We calculated the air-sea oxygen flux using both the *Liang et al.* [2013] and *Wanninkhof* [1992] gas exchange parameterizations. Bubbles are an important air-sea gas exchange mechanism for insoluble gases such as oxygen [*Woolf*, 1997; *Woolf and Thorpe,* 1991]. We chose the *Liang et al.* [2013] parameterization over others that include bubbles [e.g. *Stanley et al.*, 2009; *Vagle et al.*, 2010; *Woolf*, 1997; *Woolf and Thorpe*, 1991], because this highly resolved model of bubbles in a Langmuir circulation best

reproduces noble gas observations [*Emerson and Bushinsky*, 2016] and matches annual net community production (ANCP) rates determined from oxygen data to rates from nitrate data [*Plant et al.*, 2015]. Our aim is not to compare a variety of gas exchange parameterizations, so we only use *Liang et al.* [2013] and compare it to one other well used parameterization that does not include bubble fluxes, *Wanninkhof* [1992].

The *Liang et al.* [2013] parameterization includes three flux components: diffusive gas exchange across the air-sea interface (F_S), bubbles that completely dissolve (F_C), and bubbles that partially dissolve (F_P). These components are parameterized from wind speed, the Schmidt number of oxygen which incorporates gas diffusivity, and the air-sea oxygen gradient. We used 6-hr cross-calibrated multi-platform (CCMP) surface vector winds on a 0.25 degree grid [*Atlas et al.*, 2011; *Wentz et al.*, 2015] nearest-neighbour interpolated to the float location. Oxygen Schmidt numbers were calculated from *Ferrell and Himmelblau* [1967] and *Sharqawy et al.* [2010]. Surface float oxygen concentrations were linearly interpolated to the 6-hourly wind speed time vector. Equilibrium oxygen concentrations were calculated using *Garcia and Gordon* [1992, 1993] and float-measured surface temperature and salinity and corrected for atmospheric pressure using 6-hourly sea level pressure data from the NCEP/NCAR Reanalysis I [*Kalnay et al.*, 1996] linearly interpolated to the float location and water vapour pressure from *Dickson et al.* [2007b]. A comprehensive description of the *Liang et al.* [2013] equations can be found in Appendix D and *Emerson and Bushinsky* [2016] Appendix A.

2.6 Column-Integrated Oxygen Inventory

To investigate the change in oxygen inventory in the Labrador Sea, we linearly interpolated the float data to a 1 m depth grid from 0 to 1900 m and then vertically integrated a 1x1x1900 m^3 column. Although Argo floats typically measure to 2000 m depths, we excluded the deepest 100 m because several profiles show an unlikely 'hook' in the oxygen data at the deepest 50 m trending towards low oxygen values (Appendix E). The cause of these hooks are still being investigated, with optode response time or bio/particle fouling being possible causes [*Virginie Thierry*, personal communication]. Therefore, we chose our column depth as 1900 m to avoid including any 'hooks' in our calculations. Argo floats typically take surface measurements at 4-6 m, so these values were extended up to 0 m during gridding. Float profiles that started deeper than 10 m or ended shallower than 1900 m were not included in inventory calculations. Profiles that started deeper than 10 m were also excluded from all analyses.

3. Oxygen Sensor Calibration

All oxygen optodes used in this study needed *in situ* calibration beyond the initial factory calibration. Typically, optodes report lower values relative to the climatology in World Ocean Atlas 2009 [*Takeshita et al.*, 2013] with mean errors on the order of 10 μmol kg^{-1} at the surface [*Johnson et al.*, 2015]. This could be due to the prevalent 'storage drift' in most oxygen optodes in which the calibration changes between leaving the factory and field deployment [*Körtzinger et al.*, 2005; *Uchida et al.*, 2008; *D'Asaro and McNeil*, 2013] or could be due to inaccurate initial calibration by the optode manufacturer.

We chose to calculate a time-dependant gain for each optode based on stable deep-layer ship-based observations, which enabled us to calibrate for both the initial 'storage drift' error and post-deployment drift. Although the majority of Argo-O_2 floats show no detectable *in situ* drift in their oxygen optodes once deployed [*Takeshita et al.*, 2013; *Bittig and Körtzinger*, 2015], four of the six optodes used in this study showed *in situ* drift rates greater than -1.5 μmol kg^{-1} yr^{-1} after deployment (Table 1), a result similar to *Bushinsky et al.* [2016]. For typical wintertime (December to April) conditions in the Labrador Sea, the average *in situ* drift for these four optodes of -2.98 μmol kg^{-1} over a year would result in a 33% overestimate of air-sea oxygen flux into the ocean. This post-deployment drift is the primary reason we chose to calibrate relative to deep ocean oxygen saturations rather than a single deployment profile. Furthermore, since Argo floats typically surface only once every 10 days, it can be difficult to obtain ship-based profiles that coincide with both the location and time of float profiles. For the four floats in this study exhibiting significant post deployment drift, the closest ship-based profile in

time and space was 3 to 70 km away and 2 to 8 days from the float profile (Appendix F). Using stable deep-layer observations allows more time points to compare ship-based *in situ* measurements to float measurements and incorporates multiple ship-based casts over several years to reduce bias between cruises. Another advantage of our stable deep-layer calibration technique is that it can be applied post-deployment and does not require special hardware such as the ability to make in-air oxygen measurements [*Bushinsky et al.*, 2016; *Johnson et al.*, 2015; *Bittig and Körtzinger*, 2015].

Since winter convection in the Labrador Sea during 1994-2015 did not reach below 1800 m, the layer between 1800-1900 m shows remarkably weak rates of year-to-year changes in temperature, salinity and dissolved oxygen. From annual May surveys of the AR7W hydrographic line by Fisheries and Oceans Canada (Figure 1), oxygen values averaged in the 1800-1900 m layer of the Labrador Sea are constant from 2003-2016, with a mean concentration of 276.5 ± 2.5 μmol kg^{-1} and oxygen saturation of 86.0 ± 0.7% (red "x"s in Figure 2). Temperature in this layer rose from an average of 3.03 ± 0.09 ºC in 2003-2005 to an average of 3.34 ± 0.17 ºC in 2014-2016. The 1800-1900 m layer mainly contains a mixture of remnant Labrador Sea Water formed during extremely deep convection in the mid-1990's and Icelandic Slope Water [*Yashayaev*, 2007; *Yashayaev et al.*, 2007a and 2007b]. Due to inevitable differences in the standard solution used to calibrate the Winkler system between cruises and even within a single cruise, we made certain assumptions about spatial and interannual variability of oceanographic properties in a layer showing weak gradients on isopycnic surfaces and monotonic temporal variability over a decadal time scale. The oxygen data from the AR7W cruises was

processed and quality controlled by Igor Yashayaev and if needed corrected using deep water properties, e.g., NEADW defined by density. To maintain consistency throughout the record, all cruise oxygen data has been processed to the WOCE/CLIVAR/GO-SHIP standards of precision and replicate agreement [*Culberson*, 1994].

For all six optodes used in this study, we fit a function to the oxygen saturation measurements at 1800-1900 m and calculated a time-dependent gain relative to the stable deep layer observations (Table 1; Appendix G). Although the *D'Asaro and McNeil* [2013] calibration was designed for storage drift, we observed a similar exponentially decaying shape in the *in situ* drift for three of the six optodes used in this study; therefore, for these optodes, we used an exponentially decaying fit function based on their work (Figure 2). A linear fit function best represented the remaining 3 optodes and was used to calculate our time-dependent gain function for those optodes, although the *in situ* drift of only one of those optodes was > 1 μmol kg^{-1} yr^{-1}. All functions were fit to oxygen saturation rather than saturation anomaly. The exponentially decaying function, $F_{e\text{-}fit}(t)$, had the form [*D'Asaro and McNeil*, 2013]:

$$F_{e-fit}(t) = C_0 \cdot \left(1 - e^{\frac{-(\delta t)}{C_1}}\right) + C_2 \tag{2}$$

while the linear fit function, $F_{l\text{-}fit}(t)$, had the form:

$$F_{l-fit}(t) = C_3 \cdot \delta t + C_4 \tag{3}$$

where δt is days since deployment. The coefficients C_0, C_1, C_2, C_3, and C_4 (Table 1) were found by minimizing the sum of the square of the differences between the fit function and the optode oxygen saturation at 1800-1900m. The average root mean squared error

(RMSE) of the functions fit to the float measured deep oxygen saturation is 0.13 % (Table 1). Float profiles that were outside the study region (Figure 1) were excluded from the fit calculation. Profiles that indicated recently oxygenated waters when convection reached deeper than 1800m and profiles with values three times the standard deviation of the mean float oxygen saturation between 1800 and 1900m were also excluded from the fit calculation. We calculated the time-dependant gain, G(t), relative to the stable deep layer observations using:

$$G(t) = \frac{So_2^{Deep}}{F_{fit}(t)} \tag{4}$$

where So_2^{Deep} is the mean oxygen saturation from the stable deep layer (1800 to 1900m) calculated only from years spanning the specific float's lifetime (Table 1), and $F_{fit}(t)$ is the fit function determined from Equation 2 or 3. We then calculated the final corrected float oxygen saturation, $So_2^{Float,Corr}$, using:

$$So_2^{Float,Corr} = G(t) \cdot So_2^{Float} \tag{5}$$

where G(t) is the gain calculated from Equation 4 and So_2^{Float} is the uncalibrated oxygen saturation from float measurements (after corrected following Section 2.2). We also considered calibrating the optodes using oxygen concentration instead of saturation; however, the difference between the two methods was negligible (Appendix H). We chose saturation as the preferred correction method because optodes measure the partial pressure of oxygen, which is linearly related to the saturation.

The corrected float oxygen saturation values fit the deep values well (Figure 2). This technique adequately corrects both the initial 'storage drift' and *in situ* drift. Our calibration technique is essentially a one-point calibration, because we calibrate to a

single reference depth. Multiple studies have shown a simple gain, rather than a gain and offset, is sufficient to correct measured optode oxygen values [*Johnson et al.*, 2015; *Bushinsky et al.*, 2016; *D'Asaro and McNeil*, 2013]. For the Labrador Sea, where oxygen values are high and the range of oxygen saturation is relatively small, a similar degree of correction is applied to both surface and deep values. This calibration technique will work best for other floats in regions with repeat hydrography to improve the reliability of the ship-based observations, relatively small vertical oxygen gradients to ensure a similar level of correction to the whole profile, and convection depths shallower than 2000 m (typical Argo profile depth).

Since we calibrate float oxygen data to ship-based observations, we use the associated standard deviation (± 2.5 μmol kg^{-1} or ± 0.7 ΔO_2%) of these ship based measurements as the error in our calibrated oxygen dataset. Errors of this magnitude result in a ± 24% error in estimated annual air-sea oxygen flux into the ocean. It is interesting to note that all floats deployed in 2011 and afterwards equipped with Aanderaa 4330 optodes showed significant *in situ* drift with an exponentially decaying shape, while floats deployed in 2004 and earlier equipped with Aanderaa 3830 optodes showed either no significant *in situ* drift or a linearly decaying drift (Appendix G).

Our calibration of float 4900494 compares well to that of *Johnson et al*. [2015] for the same float using an in-air calibration method. Many recent optode calibration studies focus on in-air oxygen measurements [*Bushinsky et al.*, 2016; *Johnson et al.*, 2015; *Bittig and Körtzinger*, 2015], which requires special hardware to enable the float to

sample the air when at the surface. The mean surface ΔO_2 difference between the *Johnson et al*. [2015] calibration and our method for float 4900494 was 0.49 ± 0.36 %, with the standard deviation arising from the drift during deployment that our method corrects (Appendix I). Although the *Johnson et al*. [2015] calibration does not correct for post-deployment drift, the in-air oxygen calibration method is capable of producing a time-dependant gain to correct for drift [*Bushinsky et al.,* 2016].

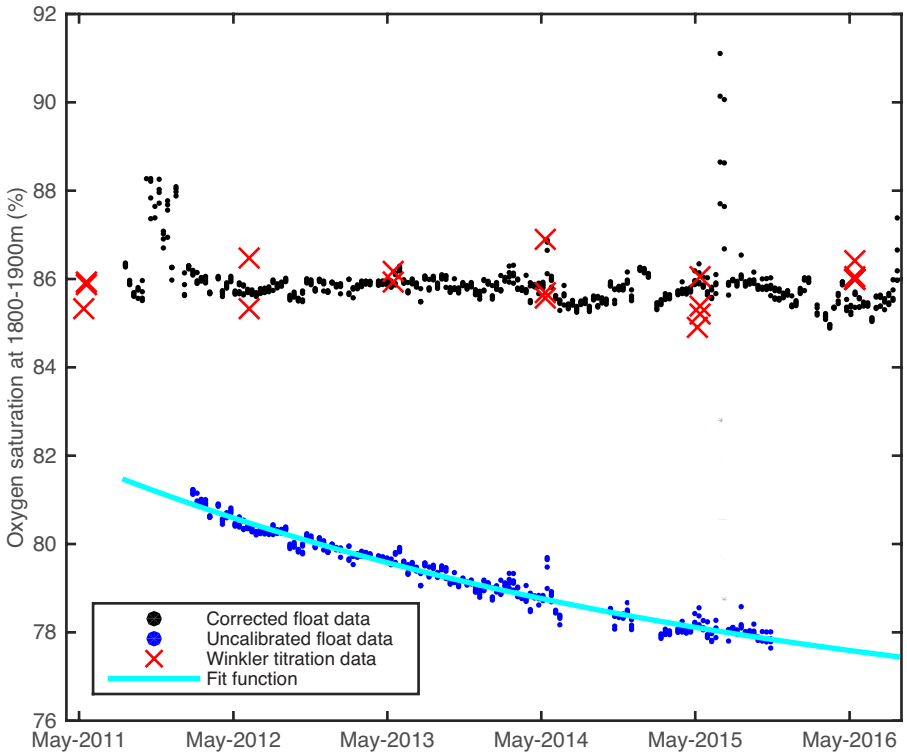

Figure 2. Float 1901210 corrected oxygen saturation (%) at 1800 to 1900 m (black dots) compared to the uncalibrated float data for the same depths used for the fit calculation (blue dots). The exponentially decaying fit function (light blue line) is calculated from Equation 2. Winkler titration data from annual May surveys of the AR7W hydrographic line is shown in red "x"s (courtesy of Igor Yashayaev).

4. Results and Discussion

4.1 Surface Annual Cycle

We use a representative year of Argo-O_2 data to explain the strong seasonal cycle in surface oxygen saturation anomaly in the Labrador Sea, stepping through each season (Figure 3). Beginning with the spring, the timing, magnitude, and location of the spring bloom in the Labrador Sea varies as a result of physical forcings such as freshwater stratification from the West Greenland Current and Greenland runoff, eddy activity, temperature, and light availability [*Frajka-Williams and Rhines*, 2010; *Körtzinger et al.*, 2008; *Wu et al.*, 2008]. However, once conditions are favourable, typically near the end of spring, a bloom leads to an increase in surface oxygen concentration and saturation anomaly (green bar in Figure 3). The oxygen concentration in the surface waters can rise by over 50 μmol kg^{-1} during this time, reaching a maximum >15% supersaturated. Surface temperatures remain cool until the start of summer when they start to rise significantly. The combined effect of the spring bloom oxygen increase and the warming waters induces outgassing of oxygen during this time period since warmer water can hold less oxygen [*Garcia and Gordon*, 1992, 1993], resulting in decreasing surface oxygen concentrations driving the surface towards equilibrium (pink bar in Figure 3). The surface temperature reaches its maximum near the end of August, which corresponds to a minimum in surface oxygen concentration.

During fall before convection, surface temperatures decrease while winds increase. As cooling occurs, surface waters becomes undersaturated and oxygen is taken

up (orange bar in Figure 3). This preconditioning phase weakens the surface stratification; however, the rising winds and cold temperatures are not strong enough to induce vigorous convection yet. Therefore a shallow mixed layer remains with the increase in oxygen concentration confined to the surface [*Lavender et al*., 2002].

During winter, continued surface cooling and increased wind speeds lead to a deepening of the mixed layer (blue bar in Figure 3). At the start of convection, the water below the surface mixed layer has a lower oxygen concentration than the surface water, and is 5% to 8% more undersaturated. As the mixed layer deepens, these oxygen undersaturated deep waters are exposed to the surface, lowering the surface oxygen concentration and saturation anomaly [*Lazier et al.*, 2002; *Pickart et al.*, 2002]. This newly exposed undersaturated water takes up oxygen from the atmosphere and is mixed downwards to be replaced by undersaturated waters from below, raising the concentration and saturation anomaly of the deep waters. However, the cooling and mixing occurs on too quick a time scale for air-sea gas exchange to bring the surface water to full equilibrium with the atmosphere [*Körtzinger et al.,* 2008], resulting in an undersaturated water mass at the end of convection. After convection, restratification occurs quickly (purple bar in Figure 3) as water from outside the convective region is advected into the well-mixed layer at various depths [*Frajka-Williams et al.*, 2014; *Körtzinger et al.,* 2004; *Lilly et al.,* 2003].

Despite complex interannual variability in the physical forcings resulting in Labrador Sea deep convection [*Yashayaev and Loder*, 2016], the seasonal cycle

described above is representative of the cycle seen in multiple floats for multiple years (Figure 4). Interannual differences seen in peak saturation anomaly (ranging from 10% to 24%) can be attributed to variability of the spring bloom [*Frajka-Williams and Rhines*, 2010]. The differences in convective undersaturation seen in Figure 4 are addressed in the next section.

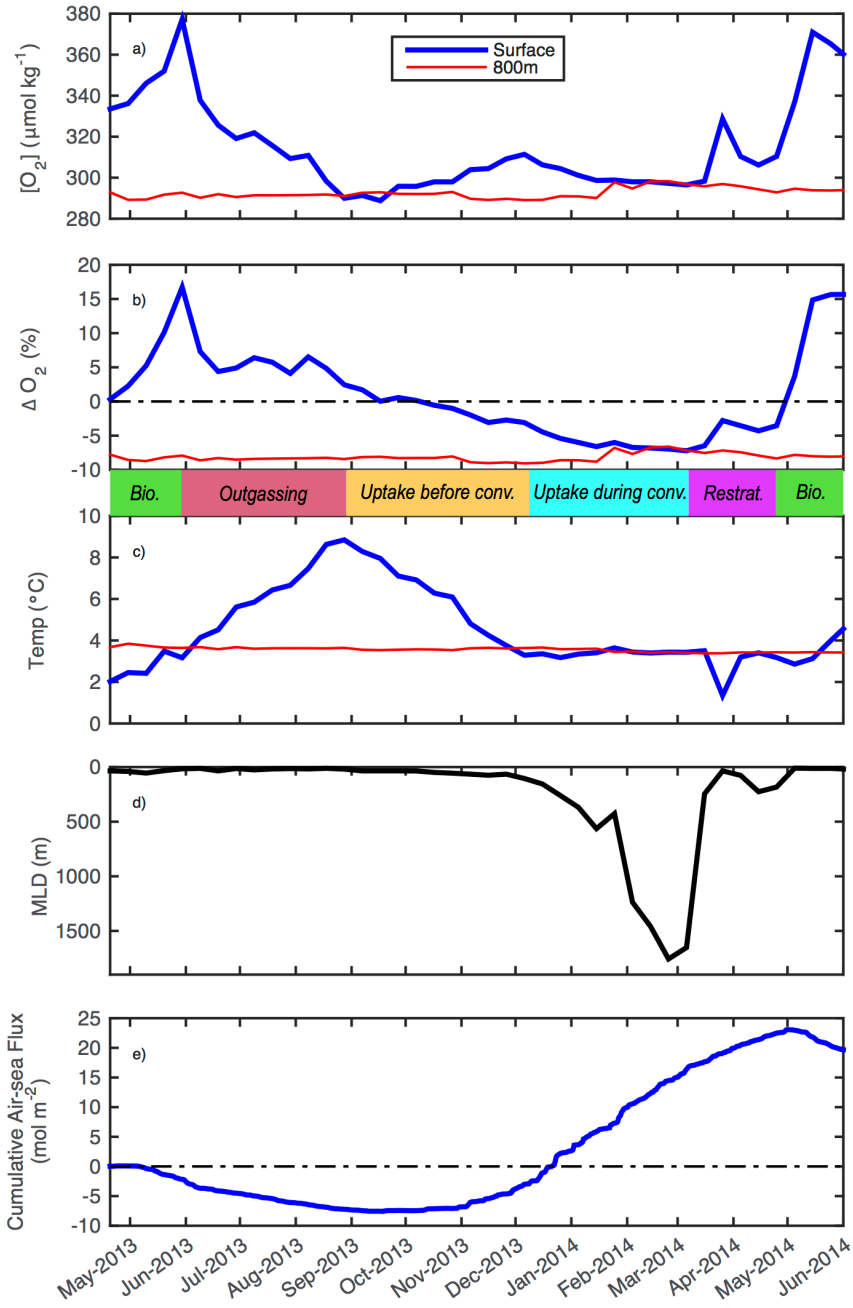

Figure 3. Seasonal cycle from spring 2013 through spring 2014 for float 1901210 of a) oxygen concentration (µmol kg^{-1}), b) oxygen saturation anomaly (%), c) temperature (°C), d) mixed layer depth (m) from *Holte et al*. [2016], and e) cumulative air-sea oxygen flux (mol m^{-2}) (blue solid line) using the *Liang et al.* [2013] gas exchange parameterization. For a), b), and c), the blue lines indicate surface values and the red lines indicate values at 800 m. The coloured bar represents time periods of (green) biological activity, (pink) outgassing, (orange) oxygen uptake before convection, (cyan) oxygen uptake during convection, and (purple) restratification.

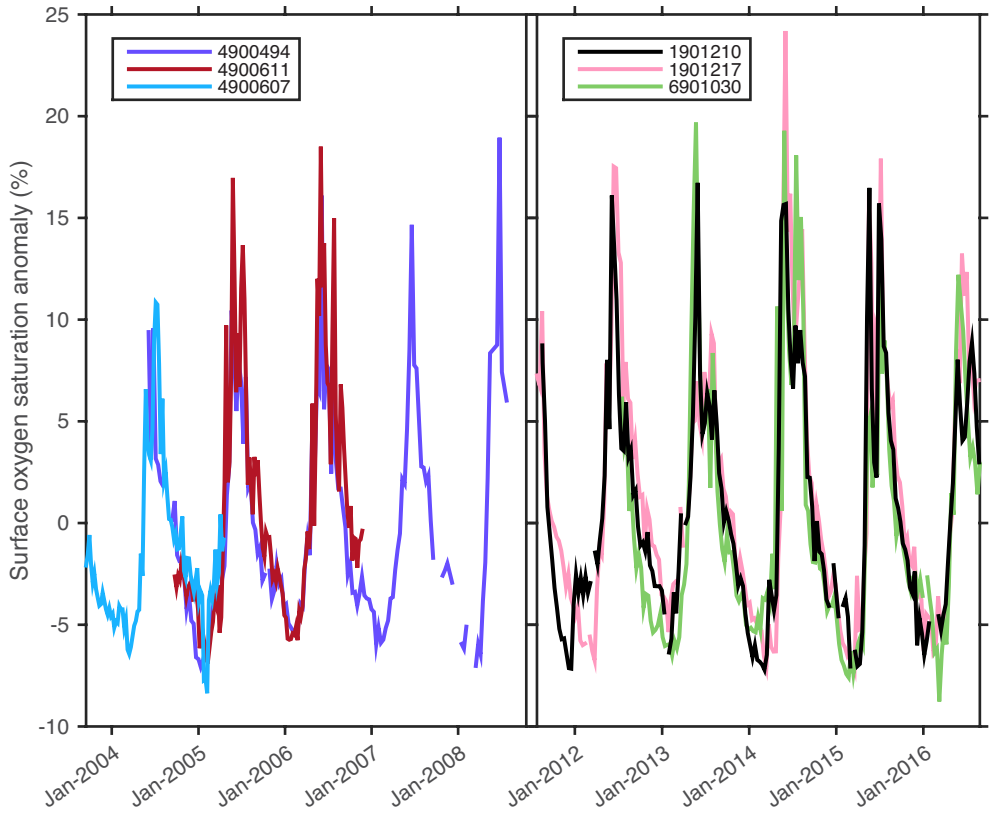

Figure 4. Time series of surface oxygen saturation anomaly (%) for all floats used in this study with float numbers in the legend. Gaps in the individual time series are due to the removal of profiles that lacked surface measurements in the upper 10 m. The time period between 2009 and late 2011 has been cut out due to lack of Argo-O_2 profile data in the region. Time series shown includes periods when floats may have drifted outside the region of interest.

4.2 Saturation at the End of Convection

At the end of convection, we found surface waters were consistently undersaturated at -6.3% to -7.6% in all cases where floats observed convection depths reached greater than 800m (blue highlighted rows in Table 2). We attribute the variation

in saturation anomaly to two factors, the date convection ended and the maximum depth of convection.

Floats that observe later convection (either because convection lasts later in a particular year or because the floats remain in the convection region longer) have oxygen saturation anomalies closer to equilibrium at the end of convection. For example in convection events deeper than 1400m, the oxygen saturation anomaly at the end of convection is closer to equilibrium when convection continues for longer (pink and purple dots in Figure 5a). As convection is prolonged, more time is available for deep undersaturated water to take up oxygen, driving the whole mixed layer slightly closer to equilibrium.

Floats that observe deeper convective events have oxygen saturation anomalies further from equilibrium. Comparing convection events of varying depths but similar end dates shows that deeper convection leads to greater undersaturation (e.g. 15 Mar in Figure 5a). During these deeper convection events, more undersaturated waters are exposed to the surface. In addition, the larger volume of the mixed layer has a larger residence time and cannot approach equilibrium quickly. Conversely, floats in regions and times when convection was limited to shallower depths have oxygen saturation anomaly values closer to equilibrium at the end of convection. With shallower convective events, less of the more highly undersaturated water is brought into the mixed layer and the smaller volume of water is able to approach equilibrium faster. In cases where the

float was not in the region of maximum convection, we observe shallower mixed layers resulted in a higher saturation anomaly, in the range of -4.1% to -6.2%.

The oxygen saturation anomalies at the end of convection we derive are consistent with ship-based measurements from two of the rare winter cruises in the Labrador Sea: values of -6% to -7% reported by *Clarke and Coote* [1988] during an early March 1976 cruise that saw convection reach 1500m, and average surface oxygen saturation anomalies of -6.1% during a February-March 1997 cruise that also saw convection reach 1500m (Knorr 147 Leg V Hydrographic Data Report).

Comparing our oxygen saturation anomalies to those of argon enables us to separate the physical and biological processes affecting oxygen. Oxygen and argon have very similar physical properties such as solubility, temperature dependence, and diffusion rates. Therefore, argon saturation anomalies are a direct estimate of the impact of physical processes (cooling, atmospheric pressure, bubbles) on oxygen. *Hamme et al.* [2017] report argon saturation anomalies in Labrador Sea Water of -1.26 ± 0.15%. The difference between the oxygen and argon saturation anomalies is approximately -5% to -6.2% and is a measure of the deep biological deficit not erased by gas exchange. The entrainment of waters during convection with low oxygen concentrations due to respiration is the main reason for the large oxygen undersaturation in the newly convected waters, rather than cooling or low atmospheric pressures.

Table 2. The end of convection oxygen saturation anomaly (%), convection end date, and maximum depth of convection observed by the floats used in this study. Also shown is the maximum depth of convection in the Labrador Sea for each given year, taken from *Yashayaev and Loder* [2016] and *Yashayaev and Loder* [2017]. Blue highlighted rows represent cases where floats observed convection greater than 800m.

Winter Year	Float ID	Convect. End Sat. Anomaly (%)	Convection End Date	Max Convect. Depth from Float (m)	Max Convect. Depth from Literature (m)
2003/2004					
	4900607	-6.07	21-Mar-04	1000	1350
2004/2005					
	4900494	-4.35	31-Mar-05	400	1150
	4900611	-5.34	23-Feb-05	600	1150
2005/2006					
	4900494	-4.12	16-Mar-06	250	1150
	4900611	-4.58	08-Mar-06	700	1150
2007/2008					
	4900494	-7.02	15-Mar-08	1590	1500
2011/2012					
	1901217	-6.29	13-Mar-12	880	1300
2012/2013					
	1901210	-5.68	08-Feb-13	400	1200
2013/2014					
	6901030	-5.15	07-Jan-14	280	1500
	1901210	-7.21	05-Mar-14	1500	1500
	1901217	-6.31	22-Apr-14	1760	1500
2014/2015					
	6901030	-7.59	21-Feb-15	1450	1650
	1901210	-6.93	09-Apr-15	1680	1650
	1901217	-7.05	18-Mar-15	1530	1650
2015/2016					
	6901030	-6.37	16-Feb-16	250	1900

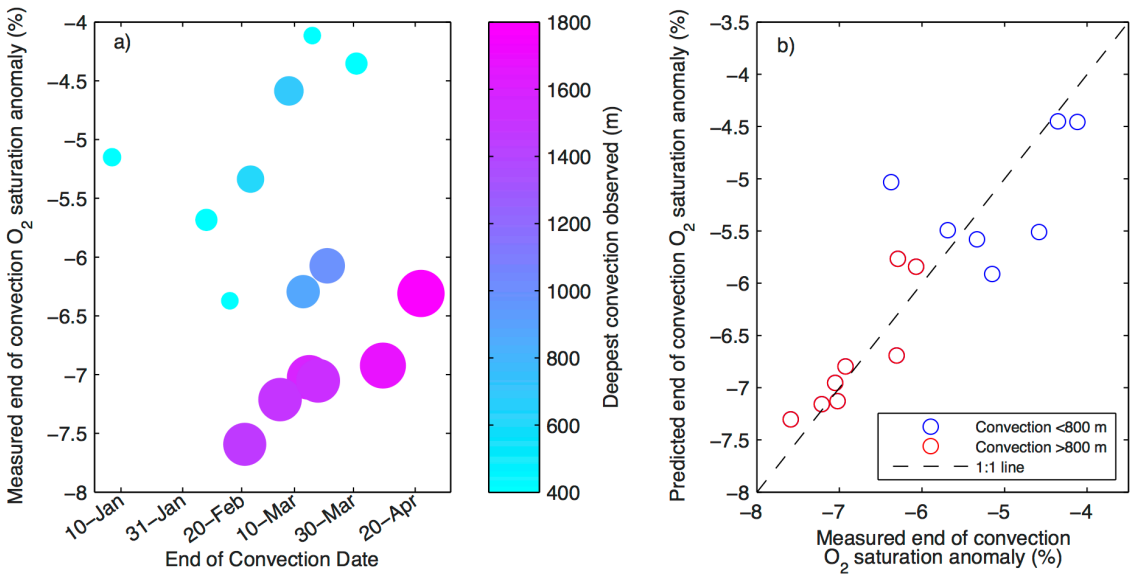

Figure 5. a) The end of convection surface oxygen saturation anomaly (%) as a function of convection end date. The colour and size of the dot represents the maximum depth of convection observed by the float (bigger and more pink is deeper, smaller and more blue is shallower). b) Predicted end of convection oxygen saturation anomaly from Equation 6 plotted against float measured end of convection oxygen saturation anomaly. Data points are separated for years where the maximum observed depth of convection was >800 m (red circles) and <800 m (blue circles).

We derive a predictive relationship for the end of convection oxygen saturation anomaly based on end of convection date and maximum observed depth of convection using multiple linear regression:

$$\Delta O_2^{predicted} = -1.9792 \times 10^{-3} \cdot Depth + 2.0466 \times 10^{-2} \cdot Yearday - 5.4991 \qquad (6)$$

where $\Delta O_2^{predicted}$ is the predicted end of convection oxygen saturation anomaly (%), *Depth* is the maximum depth of convection observed by the float (m), *Yearday* is the end date of convection expressed as day of the year. This relationship shows high skill in predicting the observed end of convection oxygen saturation anomaly, with an RMSE

between the predicted and observed end of convection oxygen saturation anomaly of 0.4319% (Figure 5b).

We also considered surface heat fluxes as a potential predictive variable, estimated from the sum of net shortwave and longwave radiation, and sensible and latent heat fluxes from the NCEP/NCAR Reanalysis I [*Kalnay et al.*, 1996]. This heat flux metric did not have as strong a correlation to the end of convection oxygen saturation anomaly as the maximum depth of convection and the end date of convection (Appendix J). Wintertime convection in the Labrador Sea depends on both the atmospheric forcing and the preconditioning of the water column [*Yashayaev and Loder*, 2017; *Schulze et al.,* 2016]. The maximum depth of convection and end date of convection capture both these factors, while heat flux ignores preconditioning.

Spatial gradients exist within the Labrador Sea during convection. Convective plumes are on the order of 1 km [*Lab Sea Group,* 1998]. Since Argo floats drift continuously, they may not observe the deepest convection even in the general convective region of the Labrador Sea during wintertime. This can be seen in Table 2 where the maximum depth of convection observed by some floats is shallower than the maximum depth of convection in the Labrador Sea from *Yashayaev and Loder* [2016] and *Yashayaev and Loder* [2017]. Furthermore, our convection end date is based on individual float observations, while convection elsewhere in the Labrador Sea may still be occurring or has already ended. Therefore, the end of convection oxygen saturation anomalies in this study are local values observed by specific floats. However, averaged

together, these local values do constrain a range expected for Labrador Sea Water as a whole.

4.3 Air-Sea Flux vs. Inventory

Uncertainties in parameterizing air-sea gas exchange limit our ability to determine the degree to which the Labrador Sea is a net sink for oxygen. The average net annual (September to September) oxygen uptake we calculate ranges from 3.1 ± 3.4 mol m^{-2} yr^{-1} using the *Wanninkhof* [1992] gas exchange parameterization to 20.3 ± 5.9 mol m^{-2} yr^{-1} using the *Liang et al.* [2013] parameterization (Figure 6, Appendix I). The *Wanninkhof* [1992] parameterization, used in many coupled ocean-atmosphere models [CMIP5, *Taylor et al.*, 2012], does not include bubble flux terms (Appendix D) and therefore likely underestimates the amount of uptake for an insoluble gas like oxygen. *Körtzinger et al.* [2008] used oxygen data from the K1 mooring in our study region (Figure 1) to estimate a range of net annual oxygen uptake from 7.7 to 11.2 mol m^{-2} yr^{-1} using a variety of gas exchange parameterizations; however, none of these included bubble flux terms and likely underestimate the oxygen uptake.

Despite large interannual variability, the average annual column-integrated oxygen inventory is near constant, as expected [*Stendardo and Gruber*, 2012]. The column-integrated oxygen inventory from 0 to 1900m (black line in Figure 6, red line in Figure 7c) shows a clear seasonality similar to the total cumulative air-sea fluxes but with a much smaller magnitude than that of the *Liang et al.* [2013] flux. We expect a difference between the cumulative air-sea flux and inventory, indicating that the Labrador

Sea is a region of net oxygen uptake, if either lateral mixing or *in situ* respiration act to reduce water column oxygen.

Lateral processes play an important role in the Labrador Sea oxygen budget. We show a clear example of this when the cumulative flux and inventory oppose each other, the flux showing increasing oxygen while the inventory is decreasing, during a restratification period after convection (Figure 7). During the beginning of this restratification, surface waters are still undersaturated driving a flux of oxygen into the ocean. However, there is a low oxygen intrusion at intermediate depths (200-700 m), driven by water that was initially outside the convection region being advected into the region (see profiles of 5 Mar 2014 and onwards in Figures 7a and 7b). Since intense vertical convection has ceased, this low oxygen intrusion reduces the column inventory despite continuous oxygen uptake at the surface. Similar low oxygen water intrusions during the restratification process occur for multiple years in other floats (Appendix B). In addition, *Körtzinger et al.* [2008, 2004] and *Frajka-Williams et al.* [2014] observe low oxygen water intrusions during the rapid restratification process. This example shows how advection can return oxygen toward lower levels rather than respiration, which in turn argues that the Labrador Sea is indeed a region of net oxygen uptake.

To quantify the lateral flux, we followed *Straneo* [2006] by considering the heat gain in the Labrador Sea during the non-convective period. The heat gained in the Labrador Sea between 200-1300 m from May to December should be due to lateral exchanges, since this layer is cut off from the surface. We find an average heat gain over

all our float data of 1.1 ± 1.3 GJ m^{-2}, similar to the *Straneo* [2006] value of 0.9 GJ m^{-2}. From this and temperature estimates of the two endmembers (newly convected Labrador Sea Water and the warmer water mass), we can determine the proportions of the outside endmember mixed into the central Labrador Sea.

Defining the outside endmember creates significant uncertainty in this analysis. Lateral exchanges between the interior of the Labrador Sea and the surrounding boundary currents and exterior basins is a complex process [*van Aken et al.,* 2011; *Gelderloos et al.,* 2011; *Katsman et al.*, 2004; *Saenko et al.*, 2014]. Constraining the mechanisms of mixing and what water is mixed into the Labrador Sea is beyond the scope of this study, so we present only a simplified calculation assuming that the outside endmember is some combination of water from the boundary currents, mainly Icelandic Slope Water (ISW) and Irminger Current (IC), and from interior exchange with the Irminger Sea (IS). Endmember properties of LSW from 200-1300 m in the central Labrador Sea for May and December were obtained from all the floats used in this study. Endmember properties for ISW, IC, and recycled LSW in the Irminger Sea were taken from floats 1901210 and 6901030 while they spent time in the Irminger Basin (Appendix L). IC contains low oxygen with a high temperature and salinity signature. The IC endmember lies on a clear temperature-salinity mixing line from the LSW May endmember to the LSW December endmember (Figure 8, Appendix L). Newly formed IS also lies close to this mixing line with slightly higher temperature and salinity than the LSW December endmember, but oxygen values somewhere in between the LSW May and December endmembers. The ISW has higher salinity and lower oxygen than the LSW endmembers, however it has

temperature values in between the LSW endmembers and does not fall on the temperature-salinity mixing line between the LSW May endmember and the LSW December endmember. We considered three scenarios for the endmember responsible for the heat gain through lateral advection observed in the Labrador Sea during the non-convective period: 1) entirely from the upper portion of the boundary current (100% IC); 2) entirely from the interior of the Irminger Sea (100% IS); and 3) 50% ISW, 25% IC, and 25% IS (mixture). We do not consider 100% ISW, since it is colder than our LSW December endmember (Figure 8) and therefore cannot be the only source of heat. We chose these first two scenarios to show that our calculation is robust to any mixing scenario between these two (entirely boundary or entirely interior).

From our simplified analysis, we find that lateral mixing and advection can account for a significant fraction of the difference between the cumulative air-sea flux and the oxygen inventory. The average fraction of the external endmember that must be mixed into the central Labrador Sea to account for the observed heat gain over May to December is 9.7 % yr^{-1} (100% IC), 64.0 % yr^{-1} (100% IS), or 33.4 % yr^{-1} (mixture). From these fractions and the endmember oxygen concentrations (Figure 8), and assuming lateral fluxes are constant year round, we calculate an annual oxygen decrease due to advection of 3.98 mol m^{-2} (100% IC), 5.64 mol m^{-2} (100% IS), or 11.34 mol m^{-2} (mixture), which accounts for 29.5 %, 41.9 %, and 84.2 % of the observed oxygen inventory decrease in the Labrador Sea from May to December respectively. These estimated lateral fluxes account for a portion of the annual average difference between the cumulative air-sea flux and the inventory, which is 22.3 ± 5.5 mol m^{-2} using the *Liang*

et al. [2013] parameterization and 5.3 ± 4.2 mol m^{-2} using the *Wanninkhof* [1992] parameterization, bringing the oxygen budget closer to balanced. Depending on the choices for mixing ratios of water masses in our outside endmember, the cumulative combination of this lateral flux and air-sea gas exchange can result in an oxygen budget that closely resembles the balanced oxygen inventory (Appendix L). This back-of-the-envelope analysis, though uncertain, strengthens our argument that advection may dominate the return of oxygen toward lower levels rather than *in situ* respiration. We conclude that the Labrador Sea is likely a region of net uptake of oxygen.

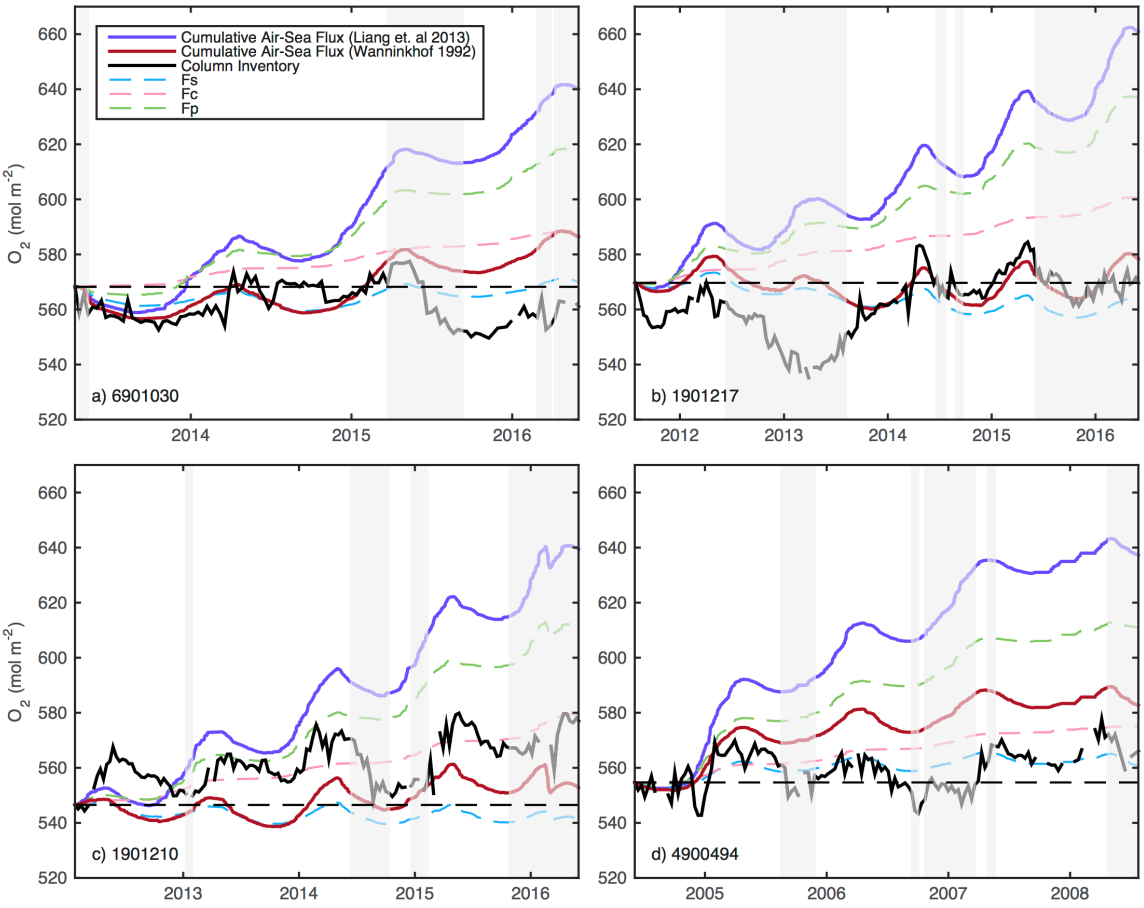

Figure 6. Time series of the cumulative air-sea flux (mol m^{-2}) calculated using the *Liang et al.* [2013] gas exchange parameterization (solid purple line) and the *Wanninkhof* [1992] parameterization (solid dark red line) compared to the oxygen column inventory from 0 to 1900 m (solid black line) for four floats (float number indicated in lower left corners). The three individual flux components of *Liang et al.* [2013] are also shown: the diffusive flux at the air-sea interface (F_S, dashed blue line), completely dissolving bubbles (F_C, dashed pink line), and partially dissolved bubbles (F_P, dashed green line). The grey shaded regions represent time periods where the float left the study region (Figure 1). Similar figures of the other two floats shown in Appendix K.

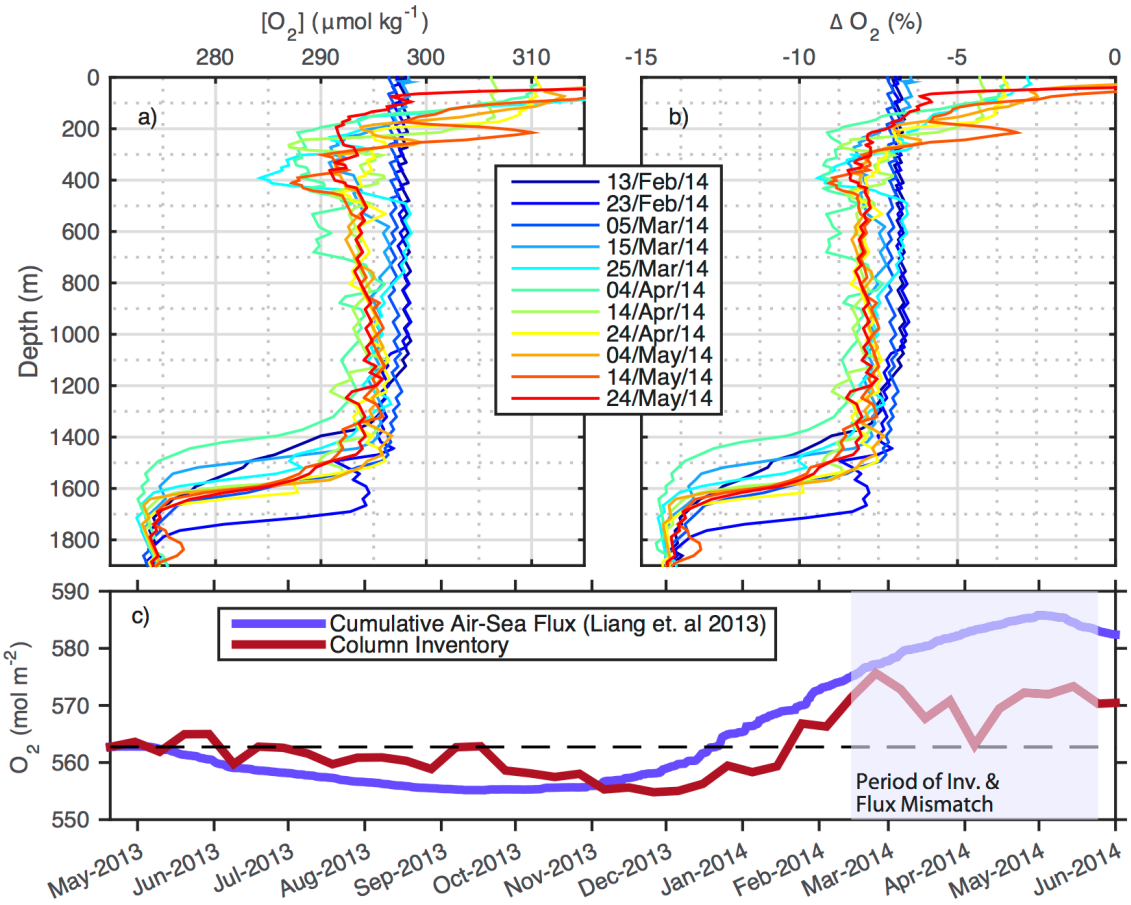

Figure 7. Evolution of (a) oxygen concentration profiles (µmol kg^{-1}) and (b) oxygen saturation anomaly profiles (%) during a time period (c, shaded blue region) when the trend in cumulative air-sea flux (mol m^{-2}) (c, solid blue line) based on *Liang et al.* [2013] differs greatly from the column inventory (c, solid red line). The jagged nature of the profiles is a result of the number of data transmitted via satellite for this Argo float.

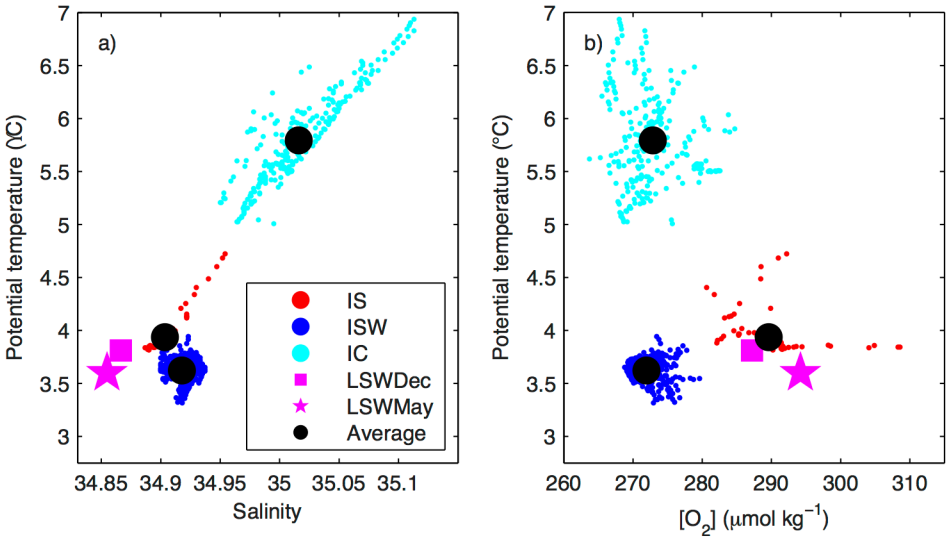

Figure 8. a) Potential temperature (°C) versus salinity and b) potential temperature versus dissolved oxygen (µmol kg^{-1}), highlighting the three water masses used as outside endmembers for the lateral flux analysis. The Irminger Sea water (IS, red circles), Icelandic Slope Water (ISW, blue circles), and the Irminger Current (IC, cyan circles) have average end member properties marked by black circles. The purple star and purple square denotes the endmember for the Labrador Sea in May (LSWMay) and December (LSWDec) respectively.

We also quantify fluxes for just the winter season. Over all observed winters from 1 November to the convection end date for individual floats, the mean column-integrated oxygen inventory change (0 to 1900 m) was 10.90 ± 7.96 mol m^{-2}, while the mean air-sea flux was 21.81 ± 7.27 mol m^{-2} from *Liang et al.* [2013] and 11.08 ± 4.49 mol m^{-2} from *Wanninkhof* [1992]. As with the annual calculations, the similarity between the inventory gain and *Wanninkhof* [1992] air-sea fluxes may be misleading, since this parameterization ignoring bubble flux terms likely underestimates the total oxygen flux and lateral processes during the convection period likely reduce the column inventory.

Our wintertime inventory changes and fluxes compare well to other work [*Körtzinger et al.*, 2004; *Koelling et al.*, 2017]. For the 2003/2004 convective period, we measure a 0-1400 m column-integrated oxygen inventory gain of 16.6 mol m^{-2} compared to the 17 mol m^{-2} found by *Körtzinger et al.* [2004], which is to be expected considering they are derived from the same float data. For the 2014/2015 convective period, we measure a 0-1700 m column-integrated oxygen inventory gain of 21.6 mol m^{-2} from the float closest to the K1 mooring compared to 24.3 mol m^{-2} found by *Koelling et al.* [2017] using K1 mooring data. Our net air-sea flux during this time was 34.2 mol m^{-2} from *Liang et al.* [2013] or 15.9 mol m^{-2} from *Wanninkhof* [1992]. The discrepancy between the two estimates of oxygen inventory changes may be due to different optode calibration methods (using an initial reference profile versus using stable deep water data), spatial gradients within the convective region, or that *Koelling et al.* [2017] used a near surface oxygen time series and an initial reference profile to diagnose inventory changes, whereas our inventory changes were directly measured every 10 days.

5. Conclusion

In this study, we found a strong correlation between the end of convection oxygen values in the Labrador Sea and the depth and end date of convection, with deeper convection and earlier end dates resulting in more undersaturated surface waters. The end of convection oxygen saturation anomaly was between -6.3% to -7.6% in all cases where convection depths reached greater than 800m. Using multiple linear regression, we produced a predictive relationship based on the depth and end date of convection. Since both the depth and end date of convection are easily obtained from standard Argo floats that measure temperature and salinity only, our relationship could be used to produce an abundant proxy dataset for end of convection saturation anomalies from standard Argo floats.

The export of oxygen undersaturated water into the ocean interior has important implications for studies using AOU, which assumes oxygen is at equilibrium with the atmosphere at the surface. For Labrador Sea water, we estimate that a 7% error in the surface oxygen concentration when calculating AOU would lead to estimates of regenerated nutrients that are 0.13 μmol kg^{-1} too high for phosphate and 2.07 μmol kg^{-1} too high for nitrate, using Redfield ratios from *Anderson and Sarmiento* [1994] of 1:16:170 for P:N:-O_2. This amounts to an overestimate of the regenerated/total nutrient ratios of 12-13%. AOU is also used to estimate the increase in interior DIC due to respiration and calcium carbonate dissolution when calculating anthropogenic carbon content. Here a 7% error in surface oxygen concentrations produces a ~14 μmol kg^{-1} error in the DIC content attributed to biological sources, based on a C:-O_2 ratio of

109:170 from *Sabine et al.* [2004]. This error does not translate into an equivalent error in anthropogenic carbon content, because the ΔC* method accounts for much of this AOU-induced error in the disequilibrium term [*Gruber et al.*, 1996], but it nevertheless represents a misattribution of the carbon source. Our findings on the degree of oxygen undersaturation after deep convection provide a correction to AOU estimates in Labrador Sea Water and an additional constraint for biogeochemical models and estimates of the global carbon budget.

Our quantification of the Labrador Sea as a net sink for oxygen varied depending on the gas exchange parameterization used, with the net annual uptake ranging from 3.1 ± 3.4 mol m^{-2} yr^{-1} to 20.3 ± 5.9 mol m^{-2} yr^{-1}. Rapid decreases in the oxygen inventory during restratification and our simplified calculation of lateral oxygen fluxes argue that horizontal advection provides low oxygen water to the region making the Labrador Sea indeed a region of net oxygen uptake. However, better constrained gas exchange parameterizations and lateral fluxes are needed to assess oxygen uptake rates. This analysis also exemplifies why treating Argo profiles in a 1-D sense can lead to misinterpretation, given that horizontal advection is transporting oxygenated waters elsewhere or the float itself is being advected. Quantifying ocean uptake of carbon dioxide is one of the most fundamental problems in chemical oceanography [e.g. *Landschützer et al.*, 2014; *Wanninkhof et al.*, 2013; *Gruber et al.*, 2009]. Constraining where and how much oxygen the ocean takes up provides window on the natural carbon cycle.

This study highlights the strengths and weaknesses of profiling floats equipped with oxygen sensors. The temporal and spatial coverage of these floats surpasses that of ship-based measurements. A more expansive float array coverage, like the new BGC-Argo Program will provide [*Biogeochemical-Argo Planning Group*, 2016], can further our knowledge of regional differences within the convective region and prevent gaps in observing convection by advection of floats outside the region. Considering the importance of horizontal advection in the region, treating Argo profiles in a 1-D sense can lead to misinterpreting oceanic processes. A large float array would build a 3-D representation of the Labrador Sea. Contrary to other studies [*Takeshita et al.*, 2013; *Bittig and Körtzinger*, 2015], the majority of our floats showed a significant *in situ* drift over time, and were corrected to stable deep-water oxygen values determined from repeat hydrography. The North Atlantic is particularly suited for this calibration technique because deep oxygen values are high (276.5 ± 2.5 μmol kg^{-1} or 86.0 ± 0.7% oxygen saturation in the targeted layer), such that a similar degree of correction is applied to both surface and deep values. Extrapolation of the applied gain to the surface may result in biases if this technique is applied to areas where deep stable values are very undersaturated. For newly deployed floats, modifications to the floats that enable in-air oxygen measurements for optode calibration [*Bushinsky et al.*, 2016; *Johnson et al.*, 2015; *Bittig and Körtzinger*, 2015] have the potential to produce accurate measurements regardless of study region.

References

Anderson, L. A., and J. L. Sarmiento (1994), Redfield ratios of remineralization determined by nutrient data analysis, *Global Biogeochemical Cycles*, 8(1), 65-80, doi:10.1029/93GB03318.

Argo (2000), *Argo float data and metadata from Global Data Assembly Centre (Argo GDAC)*. SEANOE. doi:10.17882/42182#48844.

Atlas, R., R. N. Hoffman, J. Ardizzone, S. M. Leidner, J. C. Jusem, D. K. Smith, and D. Gombos (2011), A cross-calibrated, multiplatform ocean surface wind velocity product for meteorological and oceanographic applications, *Bulletin of the American Meteorological Society*, 92, 157-174. doi:10.1175/2010BAMS2946.1.

Azetsu-Scott, K., A. Clarke, K. Falkner, J. Hamilton, E. P. Jones, C. Lee, B. Petrie, S. Prinsenberg, M. Starr, and P. Yeats (2010), Calcium carbonate saturation states in the waters of the Canadian Arctic Archipelago and the Labrador Sea, *Journal of Geophysical Research*, 115, C11021, doi:10.1029/2009JC005917.

Azetsu-Scott, K., E. P. Jones, I. Yashayaev, and R. M. Gershey (2003), Time series study of CFC concentrations in the Labrador Sea during deep and shallow convection regimes (1991–2000), *Journal of Geophysical Research*, 108, 3354, doi:10.1029/2002JC001317, C11.

Biogeochemical-Argo Planning Group (2016), *The scientific rationale, design and Implementation Plan for a Biogeochemical-Argo float array.* Edited by Ken Johnson and Hervé Claustre. doi:10.13155/46601.

Bittig, H. C., and A. Körtzinger (2015), Tackling Oxygen Optode Drift: Near-Surface and In-Air Oxygen Optode Measurements on a Float Provide an Accurate in Situ Reference, *Journal of Atmospheric and Oceanic Technology*, *32*(8), 1536-1543, doi:10.1175/jtech-d-14-00162.1.

Bittig, H. C., B. Fiedler, P. Fietzek, and A. Körtzinger (2015), Pressure Response of Aanderaa and Sea-Bird Oxygen Optodes, *Journal of Atmospheric and Oceanic Technology*, *32*(12), 2305-2317, doi:10.1175/jtechd-15-0108.1.

Böning, C. W., E. Behrens, A. Biastoch, K. Getzlaff, and J. L. Bamber (2016), Emerging impact of Greenland meltwater on deepwater formation in the North Atlantic Ocean, *Nature Geoscience*, 9(7), 523–527, doi:10.1038/ngeo2740.

Broecker, W. S., and T.-H. Peng (1982), *Tracers in the Sea*, Lamont-Doherty Earth Observatory, Palisades, N. Y. doi:10.1016/0016-7037(83)90075-3.

Bushinsky, S. M., S. R. Emerson, S. C. Riser, and D. D. Swift (2016), Accurate oxygen

measurements on modified Argo floats using in situ air calibrations, *Limnology and Oceanography: Methods*, *14*, 491-505, doi:10.1002/lom3.10107.

Carlson, C. A., D. A. Hansell, N. B. Nelson, D. A. Siegel, W. M. J. Smethie, S. Khatiwala, M. M. Meyers, and E. Halewood (2010), Dissolved organic carbon export and subsequent remineralization in the mesopelagic and bathypelagic realms of the North Atlantic basin, *Deep-Sea Research Part II*, 57, 1433–1445. doi:10.1016/j.dsr2.2010.02.013.

Clarke, R. A., and A. R. Coote (1988), The Formation of Labrador Sea Water. Part III: The Evolution of Oxygen and Nutrient Concentration, *Journal of Physical Oceanography*, 18, 469–480. doi:10.1175/1520-0485(1988)018<0469:TFOLSW>2.0.CO;2.

Cowie, G. L., J. I. Hedges, F. G. Prahl, G. J. De Lange (1995), Elemental and major biochemical changes across an oxidation front in a relict turbidite: a clear-cut oxygen effect, *Geochimica et Cosmochimica Acta,* 59, 33-46. doi: 10.1016/0016-7037(94)00329-K.

Culberson, C. H. (1994) Dissolved oxygen, in *WOCE Operations Manual*, Volume 3, Section 1, Part 3: WHP Operations and Methods, WHP Office Report WHPO 91-1, WOCE Report No. 68/91, Woods Hole Oceanographic Institute, Woods Hole, Massachusetts.

D'Asaro, E. A., and C. McNeil (2013), Calibration and stability of oxygen sensors on autonomous floats, *Journal of Atmospheric and Oceanic Technology*, 30(8), 1896–1906, doi:10.1175/JTECH-D-12-00222.1.

DeGrandpre, M.D., A. Körtzinger, U. Send, D. W. R. Wallace, and R. G. J. Bellerby, (2006), Uptake and sequestration of atmospheric CO_2 in the Labrador Sea deep convection region, *Geophysical Research Letters,* 33: doi:10.1029/2006GL026881. issn: 0094-8276.

Dickson, R. R., B. Rudels, S. Dye, M. Karcher, J. Meincke, and I. Yashayaev (2007a), Current estimates of freshwater flux through Arctic and subarctic seas, *Progress in Oceanography*, 73, 210–230. doi:10.1016/j.pocean.2006.12.003.

Dickson, A. G., C. L. Sabine, J. R. Christian (2007b), *Guide to Best Practices for Ocean CO_2 Measurements,* PICES Special Publication 3, 191pp. North Pacific Marine Science Organization, Sidney, British Columbia. http://hdl.handle.net/11329/249.

Duteil, O., W. Koeve, A. Oschlies, D. Bianchi, E. Galbraith, I. Kriest, and R. Matear (2013), A novel estimate of ocean oxygen utilisation points to a reduced rate of respiration in the ocean interior, *Biogeosciences*, 10, 7723-7738, doi:10.5194/bg-10-7723-2013.

Duteil, O., W. Koeve, A. Oschlies, O. Aumont, D. Bianchi, L. Bopp, E. Galbraith, R. Matear, J. K. Moore, J. L. Sarmiento, and J. Segschneider (2012), Preformed and regenerated phosphate in ocean general circulation models: can right total concentrations be wrong?, *Biogeosciences*, 9, 1797-1807, doi:10.5194/bg-9-1797-2012.

Emerson, S. and J. Hedges (2008), *Chemical Oceanography and the Marine Carbon Cycle*: 6th printing. Cambridge University Press. ISBN: 9780521833134.

Emerson, S., and S. Bushinsky (2016), The role of bubbles during air-sea gas exchange, *Journal of Geophysical Research: Oceans*, 121, 4360–4376, doi:10.1002/2016JC011744.

Ferrell, R. T. and D. M. Himmelblau (1967), Diffusion coefficients of nitrogen and oxygen in water, *Journal of Chemical & Engineering Data*, 12(1), 111-115, doi:10.1021/je60032a036.

Frajka-Williams, E., and P. B. Rhines (2010), Physical controls and interannual variability of the Labrador Sea spring phytoplankton bloom in distinct regions, *Deep Sea Research Part I*, 57 (2010) 541-552. doi:10.1016/j.dsr.2010.01.003.

Frajka-Williams, E., P. B. Rhines, and C. C. Eriksen (2014), Horizontal stratification during Deep Convection in the Labrador Sea, *Journal of Physical Oceanogr*aphy 44(1):220-228. doi:10.1175/JPO-D-13-069.1.

Garcia, H. E., and L. I. Gordon (1992), Oxygen solubility in seawater: Better fitting equations, *Limnology and Oceanography*, 37, 1307–1312, doi:10.4319/lo.1992.37.6.1307.

Garcia, H.E., and L.I. Gordon (1993), Erratum: Oxygen solubility in seawater: better fitting equations, *Limnology and Oceanography*, 38, 656.

Gelderloos, R., C. A. Katsman, and S. S. Drijhout (2011), Assessing the roles of three eddytypes in restratifying the Labrador Sea after deep convection, *Journal of Physical Oceanography*, 41, 2102-2119. doi:10.1175/JPO-D-11-054.1.

Gilbert, D. (2017), Environmental science: Oceans lose oxygen, *Nature*, 542, 303–304. doi:10.1038/542303a.

Gilbert, D., N. N. Rabalais, R. J. Diaz, and J. Zhang (2010), Evidence for greater oxygen decline rates in the coastal ocean than in the open ocean, *Biogeosciences*, 7(7), 2283–2296, doi:10.5194/bg-7-2283-2010.

Gruber, N., M. Gloor, S. E. Mikaloff Fletcher, S. C. Doney, S. Dutkiewicz, M. J. Follows, M. Gerber, A. R. Jacobson, F. Joos, K. Lindsay, D. Menemenlis, A. Mouchet, S. A. Müller, J. L. Sarmiento, and T. Takahashi (2009), Oceanic

sources, sinks, and transport of atmospheric CO_2, *Global Biogeochemical Cycles,* 23, GB1005, doi:10.1029/2008GB003349.

Gruber, N., J. L. Sarmiento, and T. F. Stocker (1996), An improved method for detecting anthropogenic CO2 in the oceans, *Global Biogeochemical Cycles*, 10(4), 809-837, doi:10.1029/96GB01608.

Hamme, R., S. R. Emerson, J. P. Severinghaus, M. C. Long, and I. Yashayaev (2017), Using noble gas measurements to derive air-sea process information and predict physical gas saturations, *submitted Geophysical Research Letters.*

Holte, J., J. Gilson, L. Talley and D. Roemmich (2016), *Argo Mixed Layers*, Scripps Institution of Oceanography/UCSD http://mixedlayer.ucsd.edu, (accessed [17/02/2017]).

Ito, T., M. J. Follows, E. A. Boyle (2004), Is AOU a good measure of respiration in the oceans? *Geophysical Research Letters*, 31, L17305, doi:10.1029/2004GL020900.

Johnson, K. S., J. N. Plant, S. C. Riser, and D. Gilbert (2015), Air Oxygen Calibration of Oxygen Optodes on a Profiling Float Array, *Journal of Atmospheric and Oceanic Technology*, *32*(11), 2160-2172, doi:10.1175/jtech-d-15-0101.1.

Johnson, K. S., W. M. Berelson, E. S. Boss, Z. Chase, H. Claustre, S. R. Emerson, N. Gruber, A. Körtzinger, M. J. Perry, and S. C. Riser (2009), Observing biogeochemical cycles at global scales with profiling floats and gliders: prospects for a global array, *Oceanography*, *22*(3), 216-225. doi:10.5670/oceanog.2009.81.

Kalnay, E., M. Kanamitsu, R. Kistler, W. Collins, D. Deaven, L. Gandin, M. Iredell, S. Saha, G. White, J. Woollen, Y. Zhu, A. Leetmaa, R. Reynolds, M. Chelliah, W. Ebisuzaki, W. Higgins, J. Janowiak, K. C. Mo, C. Ropelewski, J. Wang, R. Jenne, and D. Joseph (1996), The NCEP/NCAR 40-year reanalysis project, *Bulletin of the American Meteorological Society*, 77, 437–471, doi:10.1175/1520-5210477(1996)077<0437:TNYRP>2.0.CO;2.

Katsman, C. A., M. A. Spall, and R. S. Pickart (2004), Boundary current eddies and their role in the restratification of the Labrador Sea, *Journal of Physical Oceanography*, 34, 1967–1983. doi:10.1175/1520-0485(2004)034<1967:BCEATR>2.0.CO;2.

Keeling, R. F., A. Körtzinger, and N. Gruber (2010), Ocean deoxygenation in a warming world, *Annual Review of Marine Science*, 2, 199–229, doi:10.1146/annurev.marine.010908.163855.

Khatiwala, S., T. Tanhua, S. Mikaloff Fletcher, M. Gerber, S. C. Doney, H. D. Graven, N. Gruber, G. A. McKinley, A. Murata, A. F. Ríos, and C. L. Sabine (2013),

Global ocean storage of anthropogenic carbon, *Biogeosciences*, 10, 2169-2191, doi:10.5194/bg-10-2169-2013.

Kieke, D., and I. Yashayaev (2015), Studies of Labrador Sea Water formation and variability in the subpolar North Atlantic in the light of international partnership and collaboration, *Progress in Oceanography*, doi:10.1016/j.pocean.2014.12.010.

Kihm, C., and A. Körtzinger (2010), Air-sea gas transfer velocity for oxygen derived from float data, *Journal of Geophysical Research: Oceans*, 115, 8, doi:10.1029/2009jc006077.

Koelling, J., U. Send, J. Karstensen, and D. W. R. Wallace (2017), Intense uptake of O_2 during 2014-15 winter convection in the Labrador Sea, *Geophysical Research Letters*, in prep.

Körtzinger, A., J. Schimanski, and U. Send (2005), High quality oxygen measurements from profiling floats: A promising new technique, *Journal of Atmospheric and Oceanic Technology*, 22(3), 302-308, doi:10.1175/jtech1701.1.

Körtzinger, A., J. Schimanski, U. Send, and D. Wallace (2004), The ocean takes a deep breath, *Science*, *306*(5700), 1337-1337, doi:10.1126/science.1102557.

Körtzinger, A., U. Send, D. W. R. Wallace, J. Kartensen, and M. DeGrandpre (2008), Seasonal cycle of O_2 and pCO_2 in the central Labrador Sea: Atmospheric, biological, and physical implications, *Global Biogeochemical Cycles*, 22, GB1014, doi:10.1029/2007GB003029.

Lab Sea Group, (1998), The Labrador Sea Deep Convection Experiment, *Bulletin of the American Meteorology Society*, 79, 2033–2058. doi:10.1175/1520-0477(1998)079<2033:TLSDCE>2.0.CO;2.

Landschützer, P., N. Gruber, D. C. E. Bakker, and U. Schuster (2014), Recent variability of the global ocean carbon sink, *Global Biogeochemical Cycles*, 28, 927–949, doi:10.1002/2014GB004853.

Lavender, K. L., R. E. Davis, and W. B. Owens (2002), Observations of open-ocean deep convection in the Labrador Sea from subsurface floats, *Journal of Physical Oceanography*, 32, 511–526. doi:10.1175/1520-0485(2002)032<0511:oooodc>2.0.co;2.

Lazier, J., R. Hendry, A. Clarke, I. Yashayaev, and P. Rhines (2002), Convection and restratification in the Labrador Sea, 1990–2000, *Deep Sea Research Part I*, 49, 1819–1835. doi:10.1016/S0967-0637(02)00064-X.

Liang, J.-H., C. Deutsch, J. C. McWilliams, B. Baschek, P. P. Sullivan, and D. Chiba (2013), Parameterizing bubble-mediated air-sea gas exchange and its effect on

ocean ventilation, *Global Biogoechemical Cycles*, 27, 894–905, doi:10.1002/gbc.20080.

Lilly, J. M., P. B. Rhines, F. Schott, K. Lavender, J. Lazier, U. Send, and E. D'Asaro (2003), Observations of the Labrador Sea eddy field, *Progress in Oceanography,* 59, 75-176, doi:10.1016/j.pocean.2003.08.013.

Martz, T. R., K. S. Johnson, and S. C. Riser (2008), Ocean metabolism observed with oxygen sensors on profiling floats in the South Pacific, *Limnology and Oceanography*, *53*(5), 2094-2111, doi:10.4319/lo.2008.53.5_part_2.2094.

Najjar, R. G., and R. F. Keeling (1997), Analysis of the mean annual cycle of the dissolved oxygen anomaly in the World Ocean, *Journal of Marine Research*, 55:117-151. doi:10.1357/0022240973224481.

Pickart, R.S., D. J. Torres, and R. A. Clarke (2002), Hydrography of the Labrador Sea during active convection, *Journal of Physical Oceanography*, 32, 428–457. doi:10.1175/1520-0485(2002)032<0428:HOTLSD>2.0.CO;2.

Plant, J. N., K. S. Johnson, C. M. Sakamoto, H. W. Jannasch, L. J. Coletti, S. C. Riser, and D. D. Swift (2016), Net community production at ocean station papa observed with nitrate and oxygen sensors on profiling floats, *Global Biogeochemical Cycles*, 30, 859–879, doi:10.1002/2015GB005349.

Prakash, S., T. M. Balakrishnan Nair, T. V. S. Udaya Bhaskar, P. Prakash, and D. Gilbert (2012), Oxycline variability in the central Arabian Sea: An Argo-oxygen study, *Journal of Sea Research*, 71, 1-8. doi:10.1016/j.seares.2012.03.003.

Riser, S. C., and K. S. Johnson (2008), Net production of oxygen in the subtropical ocean, *Nature*, *451*(7176), 323-325, doi:10.1038/Nature06441.

Sabine, C. L., R. A. Feely, N. Gruber, R. M. Key, K. Lee, J. L. Bullister, R. Wanninkhof, C. S. Wong, D. W. R. Wallace, B. Tilbrook, F. J. Millero, T.-H. Peng, A. Kozyr, T. Ono, and A. F. Rios (2004), The Oceanic Sink for Anthropogenic CO_2, *Science* 305, no. 5682: 367-71. doi:10.1126/science.1097403.

Saenko, O. A., F. Dupont, D. Yang, P. G. Myers, I. Yashayaev, and G. C. Smith (2014), Role of resolved and parameterized eddies in the Labrador Sea balance of heat and buoyancy, *Journal of Physical Oceanography*, 44, 3008-3032, doi:10.1175/JPO-D-14-0041.1.

Schulze, L. M., R. S. Pickart, and G. W. K. Moore (2016), Atmospheric forcing during active convection in the Labrador Sea and its impact on mixed-layer depth, *Journal of Geophysical Research: Oceans*, 121, 6978–6992, doi:10.1002/2015JC011607.

Sharqawy, M. H., J. H. Lienhard V, and S. M. Zubair (2010), Desalination and Water Treatment, 16, 354-380. (http://web.mit.edu/seawater/).

Stanley, R., W. Jenkins, D. Lott, and S. Doney (2009), Noble gas constraints on air-sea gas exchange and bubble fluxes, *Journal of Geophysical Research*, 114, C11020, doi:10.1029/2009JC005396.

Steinfeldt, R., M. Rhein, J. L. Bullister, and T. Tanhua (2009), Inventory changes in anthropogenic carbon from 1997–2003 in the Atlantic Ocean between 20°S and 65°N, *Global Biogeochemical Cycles*, 23, GB3010, doi:10.1029/2008GB003311.

Stendardo, I., and N. Gruber (2012), Oxygen trends over five decades in the North Atlantic, *Journal Geophysical Research*, 117, C11004, doi:10.1029/2012JC007909.

Straneo, F. (2006), Heat and freshwater transport through the central Labrador Sea, *Journal of Physical Oceanography*, 36, 606-628. doi:10.1175/JPO2875.1.

Takeshita, Y., T. R. Martz, K. S. Johnson, J. N. Plant, D. Gilbert, S. C. Riser, C. Neill, and B. Tilbrook (2013), A climatology‐based quality control procedure for profiling float oxygen data, *Journal of Geophysical Research: Oceans*, 118(10), 5640-5650. doi:10.1002/jgrc.20399.

Taylor, K. E., R. J. Stouffer, and G. A. Meehl (2012), An overview of cmip5 and the experiment design, *Bulletin of the American Meteorological Society*, 93, 485-498, doi: 626 10.1175/BAMS-D-11-00094.1.

Tengberg, A., J. Hovdenes, H. Andersson, O. Brocandel, R. Diaz, D. Hebert, and A. Stangelmayer (2006), Evaluation of a lifetimebased optode to measure oxygen in aquatic systems. *Limnology and Oceanography: Methods,* 4, 7-17 doi:10.4319/lom.2006.4.7.

Thierry, V., D. Gilbert, T. Kobayashi, and C. Schmid (2013), Processing Argo oxygen data at the DAC level, version 1.3. Argo Data Management, 20 pp. [Available online at http://www.argodatamgt.org/content/download/16300/106561/file/ARGO_oxygen_proposition_v1p3.pdf.].

Thierry, V., D. Gilbert, T. Kobayashi, C. Schmid, and S. Kanako (2016), *Processing Argo oxygen data at the DAC level cookbook.* doi:10.13155/39795.

Uchida, H., T. Kawano, I. Kaneko, and M. Fukasawa (2008), In situ calibration of optode-based oxygen sensors, *Journal of Atmospheric and Oceanic Technology*, 25, 2271–2281, doi:10.1175/2008JTECHO549.1.

Vagle, S., C. McNeil, and N. Steiner (2010), Upper ocean bubble measurements from the

NE Pacific and estimates of their role in air-sea gas transfer of the weakly soluble gases nitrogen and oxygen, *Journal of Geophysical Research*, 115, C12054, doi:10.1029/2009JC005990.

van Aken, H. M., M. F. de Jong, and I. Yashayaev (2011), Decadal and multi-decadal variability of Labrador Sea Water in the north-western North Atlantic Ocean derived from tracer distributions: Heat budget, ventilation, and advection, *Deep Sea Research Part I,* 58(5), 505-523. doi:10.1016/j.dsr.2011.02.008.

Wanninkhof, R., G.-H. Park, T. Takahashi, C. Sweeney, R. Feely, Y. Nojiri, N. Gruber, S. C. Doney, G. A. McKinley, A. Lenton, C. Le Quéré, C. Heinze, J. Schwinger, H. Graven, and S. Khatiwala (2013), Global ocean carbon uptake: magnitude, variability and trends, *Biogeosciences*, 10, 1983-2000, doi:10.5194/bg-10-1983-2013.

Wanninkhof, R. (1992), Relationship between wind speed and gas exchange over the ocean, *Journal of Geophysical Research*, 97(C5), 7373–7382. doi:10.1029/92JC00188.

Wentz, F.J., J. Scott, R. Hoffman, M. Leidner, R. Atlas, J. Ardizzone (2015), Remote Sensing Systems Cross-Calibrated Multi-Platform (CCMP) 6-hourly ocean vector wind analysis product on 0.25 deg grid, Version 2.0. Remote Sensing Systems, Santa Rosa, CA. Available online at www.remss.com/measurements/ccmp. [Accessed 19 Dec 2016].

Woolf, D. K. (1997), Bubbles and their role in gas exchange, in *The Sea Surface and Global Change*, edited by P. S. Liss and R. A. Duce, pp. 173–206, Cambridge Univ. Press, N. Y., doi:10.1017/CBO9780511525025.007.

Woolf, D. K., and S. Thorpe (1991), Bubbles and the air-sea exchange of gases in near saturation conditions, *Journal of Marine Research*, 49, 435–466, doi:10.1357/002224091784995765.

Wu, Y.S., T. Platt, C. C. L. Tang, and S. Sathyendranath (2008), Regional differences in the timing of the spring bloom in the Labrador Sea, *Marine Ecology Progress* Series 355, 9–20. doi:10.3354/meps07233.

Yashayaev, I. (2007), Hydrographic changes in the Labrador Sea, 1960–2005, *Progress in Oceanography*, 73(3-4), 242–276. doi:10.1016/j.pocean.2007.04.015.

Yashayaev, I., and J. W. Loder (2016), Recurrent replenishment of Labrador Sea Water and associated decadal-scale variability, *Journal of Geophysical Research Oceans*, 121, doi:10.1002/2016JC012046.

Yashayaev, I., and J. W. Loder (2017), Further intensification of deep convection in the Labrador Sea in 2016, *Geophysical Research Letters*, 44, 1429–1438, doi:10.1002/2016GL071668.

Yashayaev, I., H. M. vanAken, N. P. Holliday, and M. Bersch (2007a), Transformation of the Labrador Sea Water in the subpolar North Atlantic, *Geophysical Research Letters*, 34, L22605, doi:10.1029/2007GL031812.

Yashayaev, I., M. Bersch, and H. M. vanAken (2007b), Spreading of the Labrador Sea Water to the Irminger and Iceland basins, *Geophysical Research Letters*, 34, L10602, doi:10.1029/2006GL028999.

Zimmerman, S., T. K. McKee, R. S. Pickart, and W. M. Smethie (2000), Knorr 147 leg V hydrographic data report: Labrador Sea Deep Convection Experiment, *WHOI-2000-05*, Woods Hole Oceanographic Institute, Woods Hole, Massachusetts, doi:10.1575/1912/58.

Appendices

Appendix A: Pressure correction

When we accessed the Argo data, raw dissolved oxygen values from floats were corrected for pressure based on *Uchida et al.,* [2008]. We updated the pressure correction to that of *Bittig et al.* [2015] when we noticed the old correction from *Uchida et al.,* [2008] showed oxygen concentration changes on average of 3.14 μmol kg^{-1} /1000 m in deeply convecting layers where we would expect the oxygen concentration to be constant (Figure A1). This new pressure correction from *Bittig et al.* [2015] is now the recommended method according to the updated "Processing Argo OXYGEN data at the DAC level, Version 2.2" manual [*Thierry et al.*, 2016].

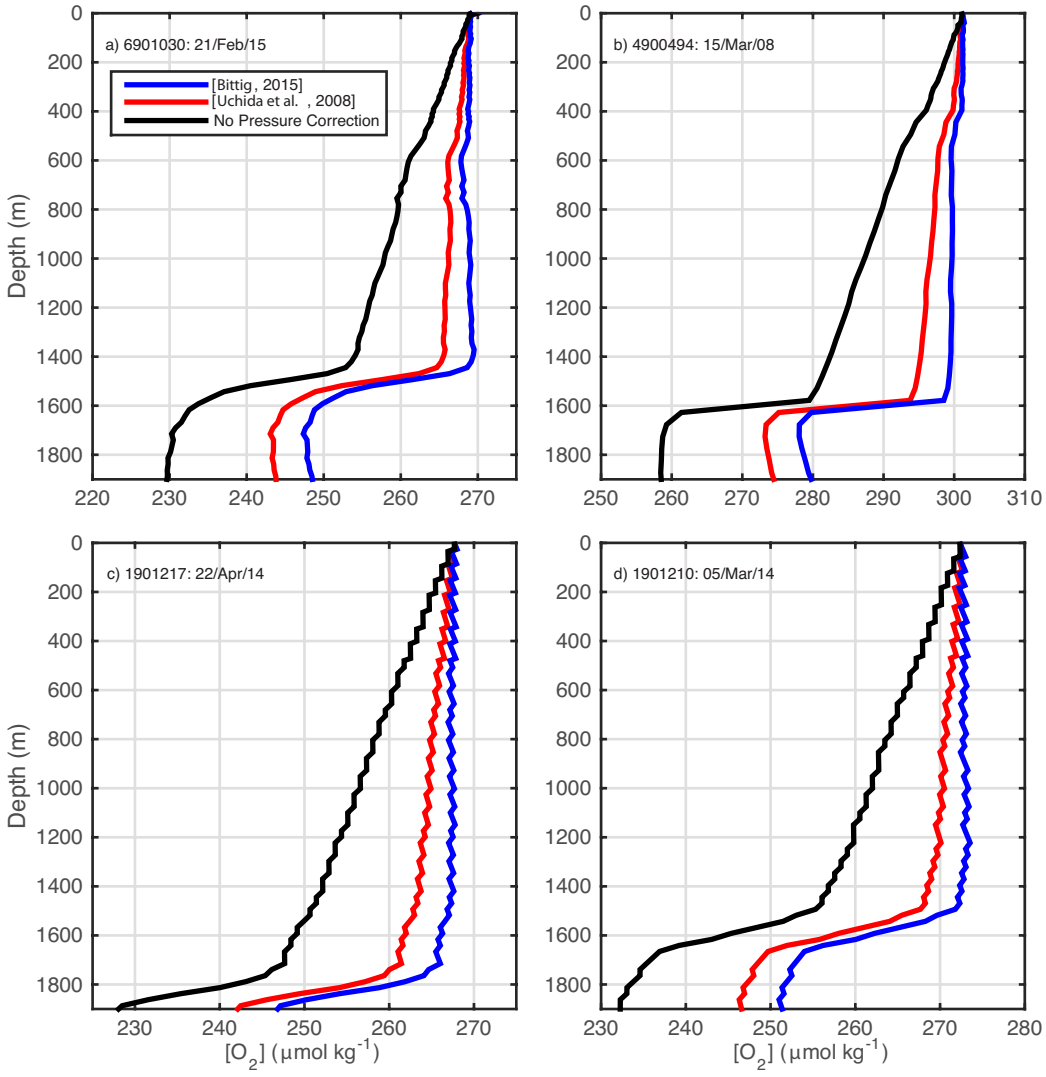

Figure A 1. Oxygen concentration profiles during deep convection with various pressure corrections applied from four floats (float number and profile date indicated in top left corners). Pressure corrections shown are based on *Bittig et al.* [2015] (blue line), or *Uchida et al.,* [2008] (red line), with data having no pressure correction shown as well (black line).

Appendix B: End of convection profile selection

Choosing the end of convection date was done visually by inspecting individual profiles of temperature, salinity, potential density, calibrated dissolved oxygen concentration, and calibrated oxygen saturation anomaly on a float-by-float and year-by-year basis. Figures B1 through B6 show the end of convection calibrated oxygen concentration and oxygen saturation anomaly profiles (in black) plus the 5 previous and 5 subsequent profiles. We chose the end of convection profile as the profile with the maximum mixed layer depth that had subsequent profiles showing some sort of restratification in the surface waters or horizontal advection of waters outside the region penetrating the profiles mid-depth.

These figures further illustrate that the majority of floats show low oxygen water intrusion during the restratification process, similar to *Körtzinger et al.* [2008, 2004] and *Frajka-Williams et al.* [2014]. These low oxygen water intrusions during the restratification period argue for advection mainly returning oxygen toward lower levels rather than in situ respiration, which in itself argues that the Labrador Sea is indeed a region of net oxygen uptake. Low oxygen water intrusions can be seen in the majority of winters from Figures B1 through B6 by looking at subsequent profiles after the end of convection (black profile).

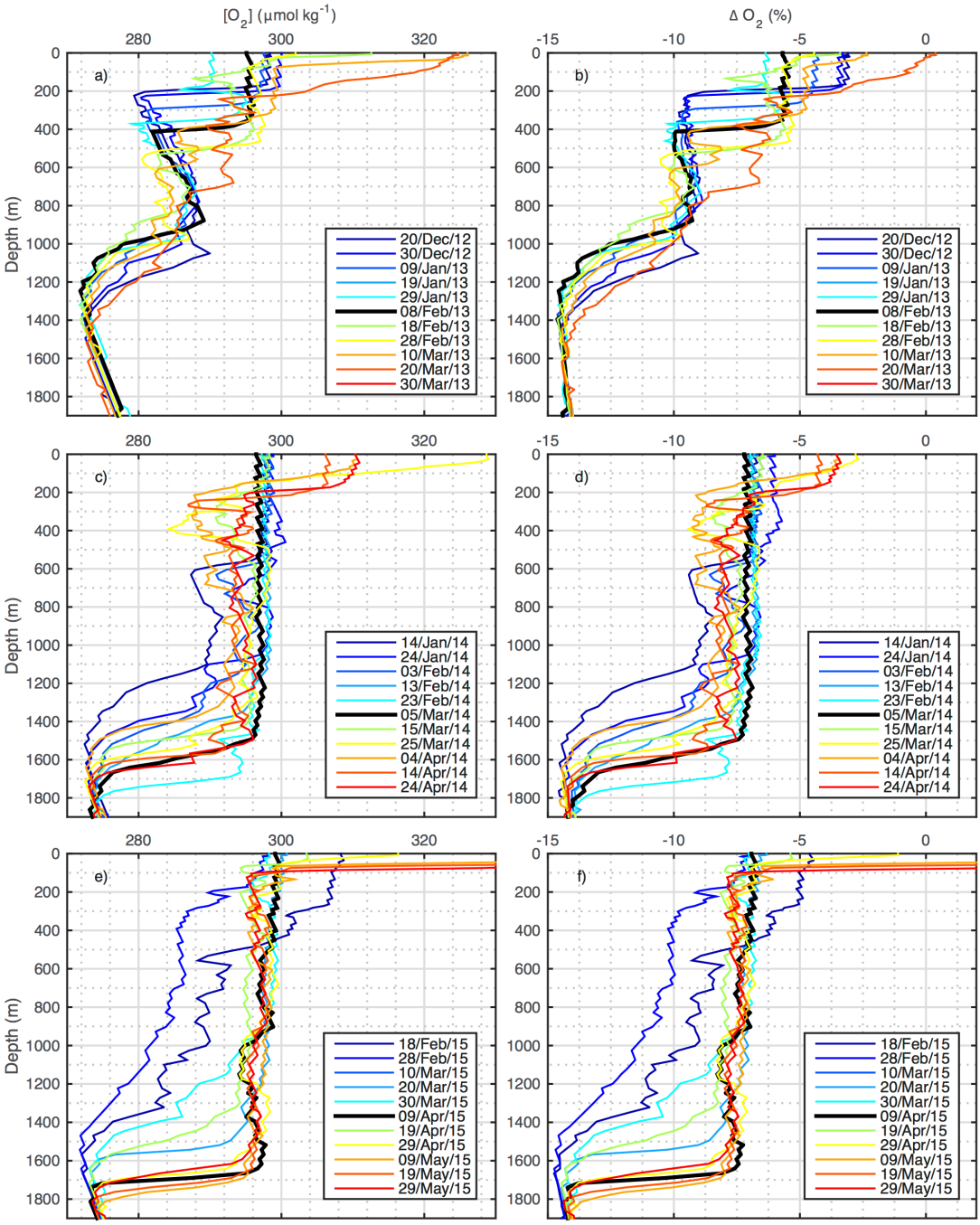

Figure B 1. Calibrated a), c), e) oxygen concentration profiles and b), d), f) oxygen saturation anomaly profiles from float 1901210 for the winter convection period indicated in the respective legend. Highlighted (black line) is the profile selected as the end of convection.

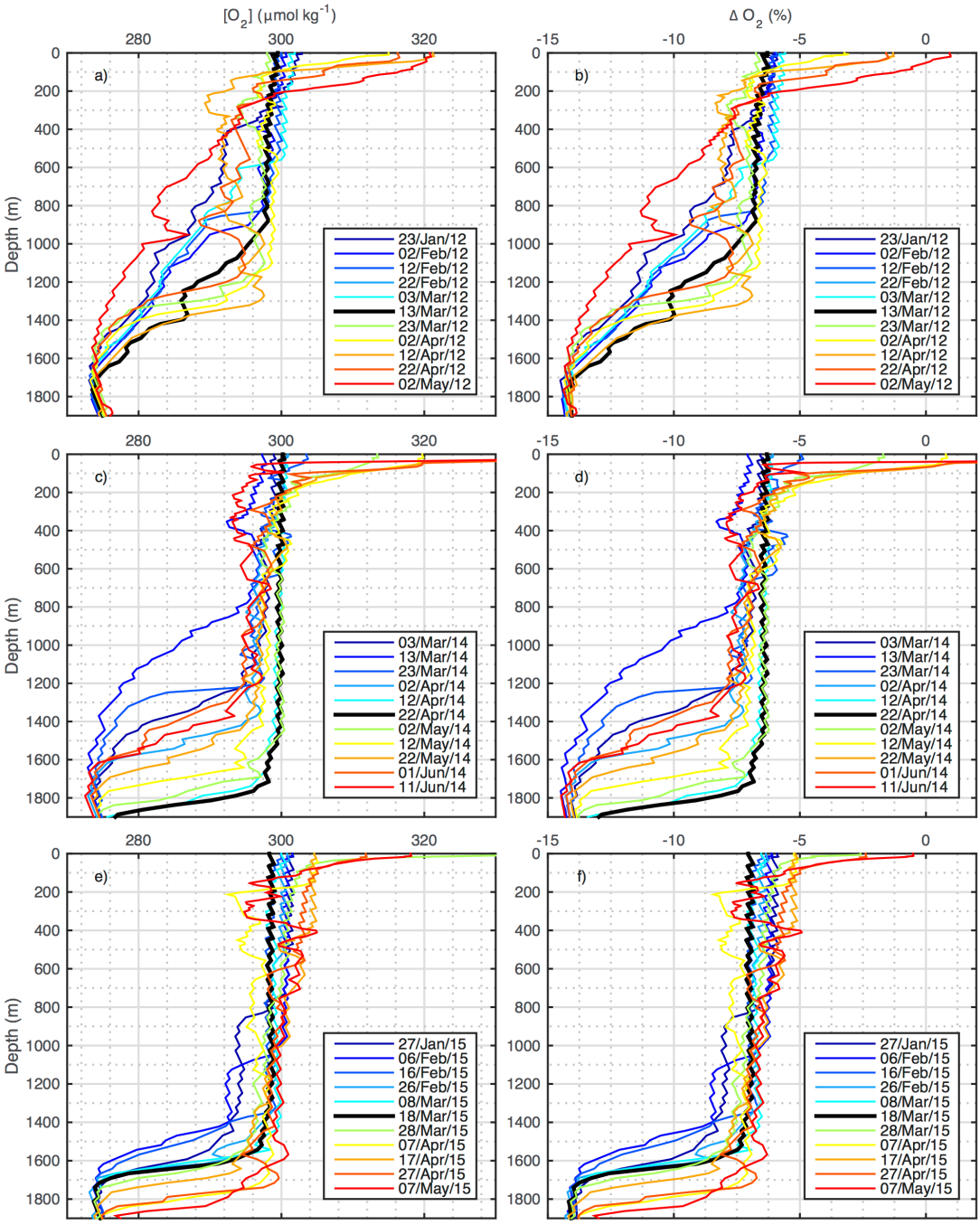

Figure B 2. Calibrated a), c), e) oxygen concentration profiles and b), d), f) oxygen saturation anomaly profiles from float 1901217 for the winter convection period indicated in the respective legend. Highlighted (black line) is the profile selected as the end of convection.

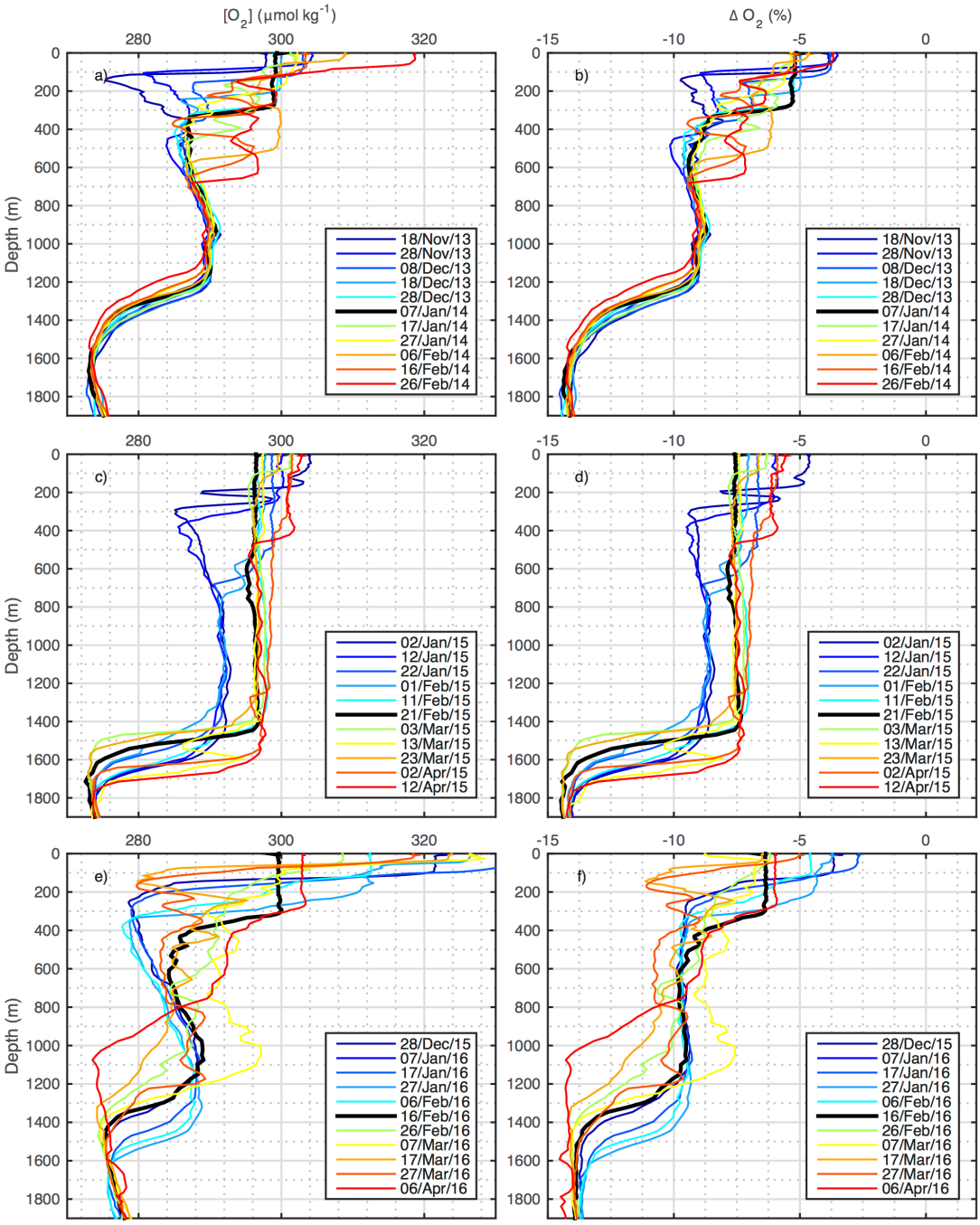

Figure B 3. Calibrated a), c), e) oxygen concentration profiles and b), d), f) oxygen saturation anomaly profiles from float 6901030 for the winter convection period indicated in the respective legend. Highlighted (black line) is the profile selected as the end of convection.

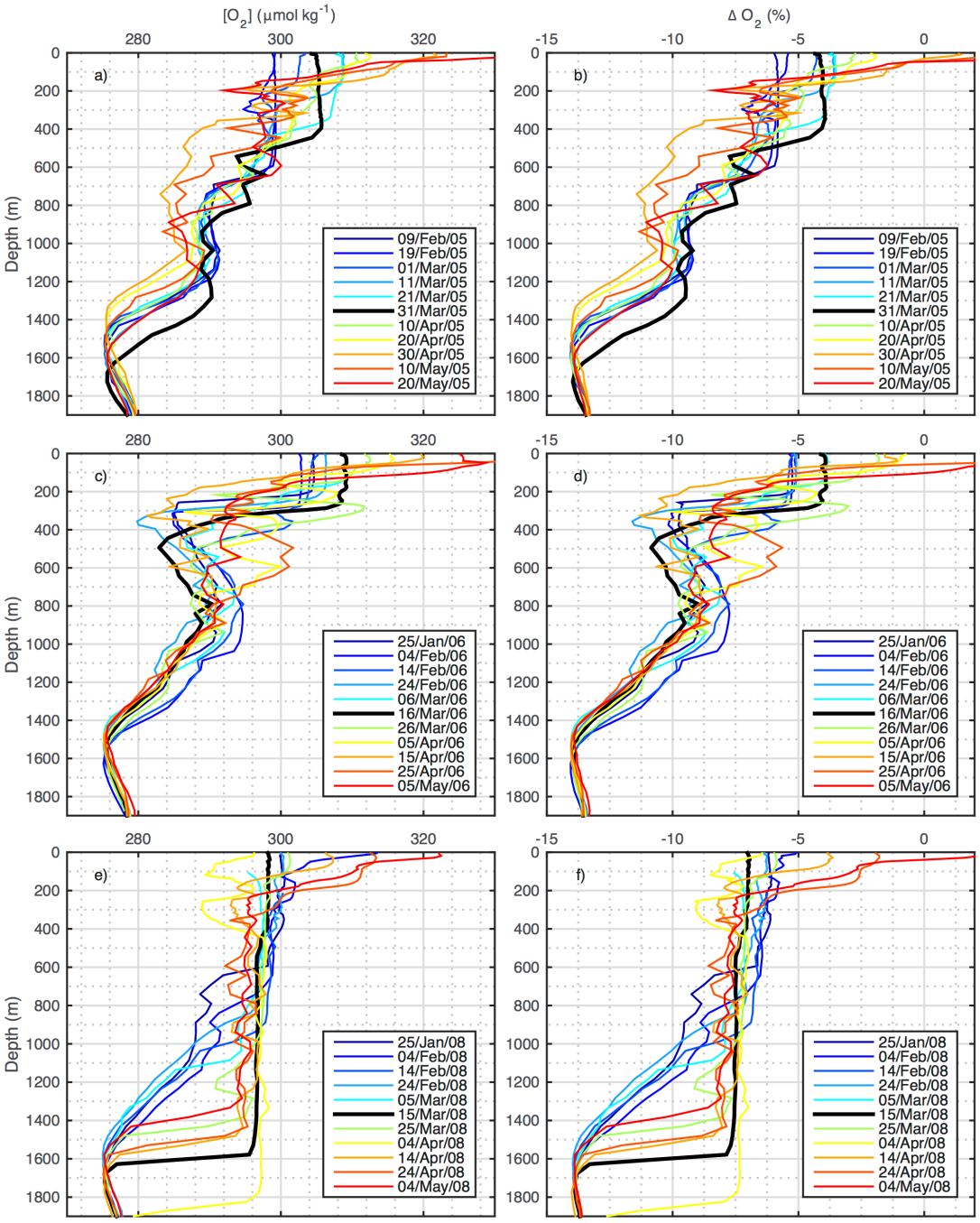

Figure B 4. Calibrated a), c), e) oxygen concentration profiles and b), d), f) oxygen saturation anomaly profiles from float 4900494 for the winter convection period indicated in the respective legend. Highlighted (black line) is the profile selected as the end of convection.

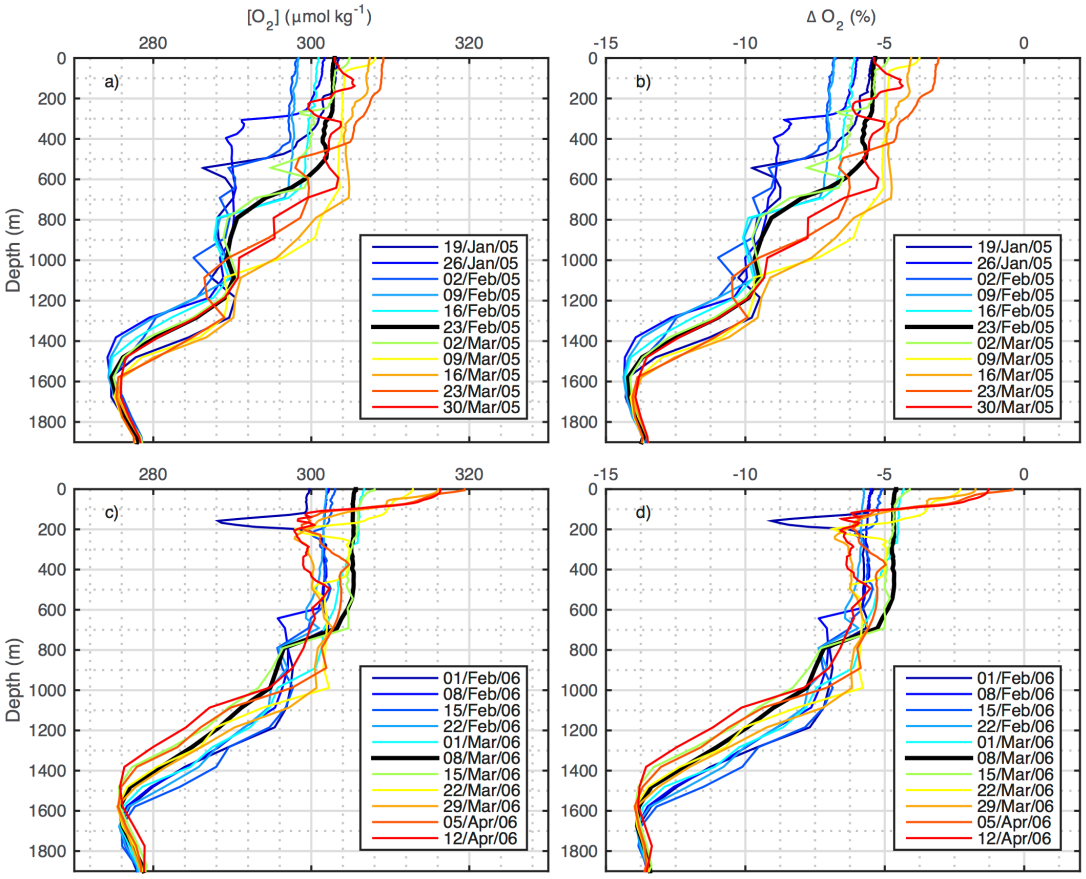

Figure B 5. Calibrated a), c) oxygen concentration profiles and b), d) oxygen saturation anomaly profiles from float 4900611 for the winter convection period indicated in the respective legend. Highlighted (black line) is the profile selected as the end of convection.

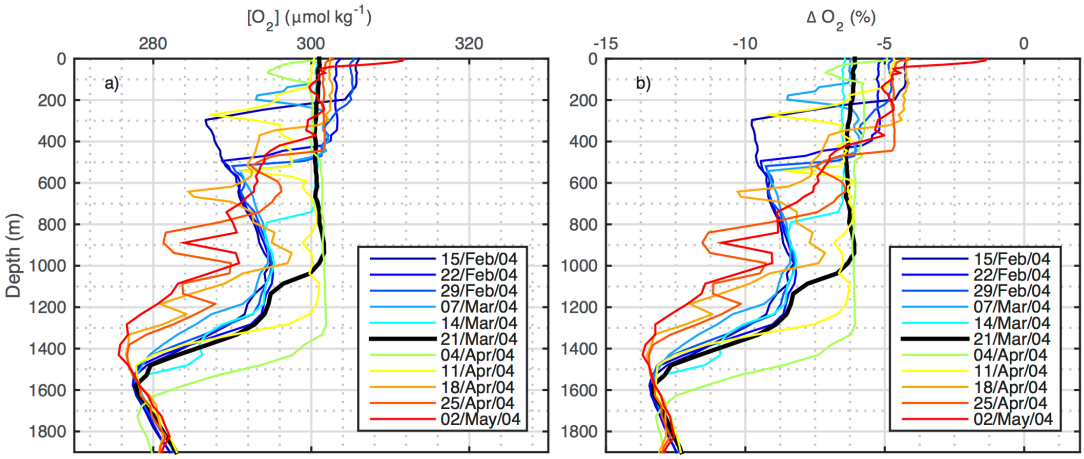

Figure B 6. Calibrated a) oxygen concentration profiles and b) oxygen saturation anomaly profiles from float 4900607 for the winter convection period indicated in the respective legend. Highlighted (black line) is the profile selected as the end of convection.

Appendix C: End of convection versus convection duration

Defining the end of convection date was needed in order to investigate the oxygen saturation anomaly at the end of convection. We also considered using convection duration as a metric, however, determining the start of convection date was more subjective. Various criteria could be used to select a start date of convection. Some example criteria could be: a mixed layer depth threshold, the time when the mixed layer starts to increase, or the time surface oxygen saturation starts to decrease from entrainment of low oxygen water from below. The start of convection date in Figure C1 was chosen as the profile in which there was a deepening of the mixed layer greater than 10 m and an increase in mixed layer potential density of ~ 0.1 kg m^{-3} in all subsequent profiles. To simplify this analysis we therefore chose to use only the end date of convection as a metric. Our results were robust to the choice of end of convection date vs. convection duration (Figure C1). The few differences that can be seen in Figure C1 arise solely from the subjective nature of choosing a convection start date.

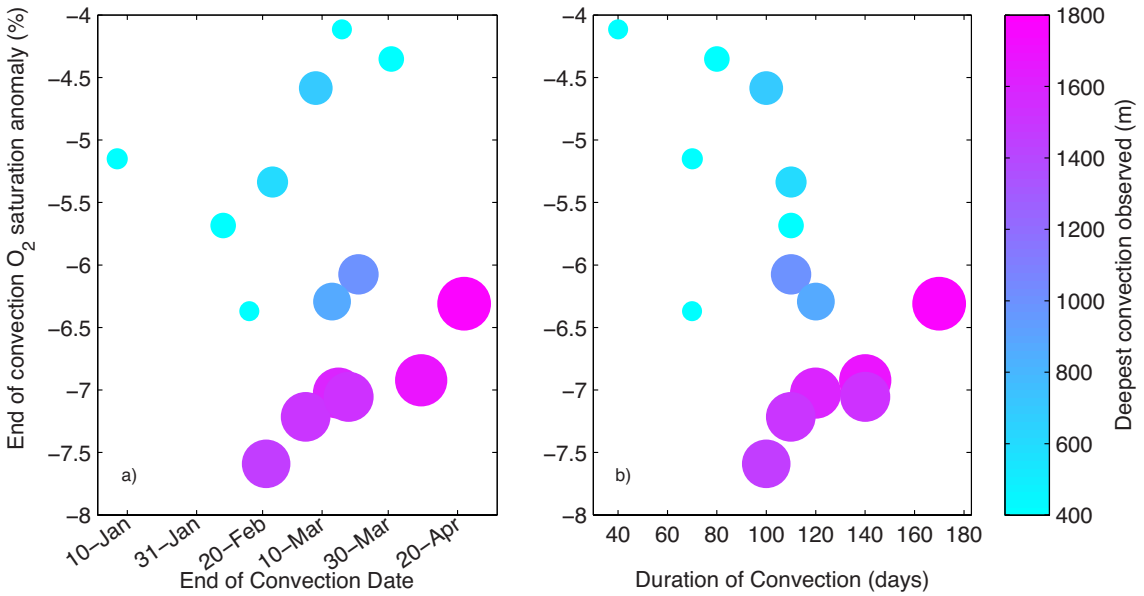

Figure C 1. The end of convection surface oxygen saturation anomaly (%) as a function of a) convection end date and b) duration of convection. The colour and size of the dot represents the maximum depth of convection observed by the float (bigger and more pink is deeper, smaller and more blue is shallower).

Appendix D: Flux equations

The *Liang et al.* [2013] parameterization is based on direct calculations of bubble induced gas fluxes from a highly resolved model of bubbles in a Langmuir circulation. The total flux is a sum of its three flux components: diffusive gas exchange across the air-sea interface (F_S), bubbles that completely dissolve (F_C), and bubbles that partially dissolve (F_P). Diffusive gas exchange across the air-sea interface in units of mol m^{-2} s^{-1} is given by:

$$F_s = k_s\left([O_2]_{eq} \cdot slpc - [O_2]_{float}\right) \qquad (\text{mol m}^{-2}\ \text{s}^{-1}) \qquad \text{(D1)}$$

where $[O_2]_{eq}$ is the oxygen concentration (in mol m^{-3}) at equilibrium with the atmosphere calculated using *Garcia and Gordon* [1992, 1993] and float measured potential temperature and salinity, $[O_2]_{float}$ is the oxygen concentration (in mol m^{-3}) at the surface measured by the float, k_s is the gas transfer velocity, and *slpc* is an atmospheric pressure correction factor to convert from reference to observed conditions. *slpc* in Equation D1 is given by:

$$slpc = \frac{slp - pH_2O(S,T)}{1 - pH_2O(S,T)} \qquad \text{(D2)}$$

where *slp* is the sea level pressure (in atm) and $pH_2O(S,T)$ is the vapor pressure of sea water at the measured salinity (S) and temperature (T). The gas transfer velocity, k_s, from Equation D1 is given by:

$$k_s = 1.3 \cdot 1.04 \cdot 10^{-4} \cdot u_*^a \left(\frac{S_c}{660}\right)^{-0.5} \qquad (\text{m s}^{-1}) \qquad \text{(D3)}$$

where S_c is the Schmidt number calculated from *Ferrell and Himmelblau* [1967] and *Sharqawy et al.* [2010] and u_*^a is the air side friction velocity given by:

$$u_*^a = \sqrt{C_d}\, u_{10} \qquad (\text{m s}^{-1}) \qquad \text{(D4)}$$

where u_{10} is the wind speed at 10 m above the air water interface and C_d is the drag coefficient expressed as:

$$C_d = \begin{cases} 0.0012 & (u_{10} < 11\ m\ s^{-1}) \\ (0.49 + 0.065u_{10}) \cdot 10^{-3} & (11 \le u_{10} \le 20\ m\ s^{-1}) \\ 0.0018 & (u_{10} > 20\ m\ s^{-1}) \end{cases} \qquad \text{(D5)}$$

For bubbles that completely dissolve, the flux (F_C) is given by:

$$F_c = 5.56 \cdot u_*^{w\,3.86} \cdot X_{O2} \qquad (\text{mol m}^{-2}\ \text{s}^{-1}) \qquad \text{(D6)}$$

where X_{O2} is the mole fraction of oxygen in air (0.20946) and u_*^w is the water-side friction velocity given by:

$$u_*^w = \sqrt{\frac{\rho_{air}}{\rho_w}} \cdot u_*^a \qquad (\text{m s}^{-1}) \qquad \text{(D7)}$$

where u_*^a is the air side friction velocity from Equation D4, ρ_w is the density of sea water measured by the float, and ρ_{air} is the density of air (1.225 kg m^{-3}).

For bubbles that partially dissolve, the flux (F_P) is given by:

$$F_p = 5.5 \cdot u_*^{w\,2.76} \cdot \left((1 + \Delta P)[O_2]_{eq} \cdot slpc - [O_2]_{float} \right) \cdot \left(\frac{S_c}{660} \right)^{-\frac{2}{3}} \qquad (\text{mol m}^{-2}\ \text{s}^{-1}) \qquad \text{(D8)}$$

where ΔP is the fractional increase in saturation concentration with pressure equal to:

$$\Delta P = 1.5244 u_*^{w\,1.06} \qquad \text{(D9)}$$

The *Wanninkhof* [1992] gas exchange parameterization is one of the most commonly used parameterization with a quadratic dependence on wind speed based on

global constraints of bomb-^{14}C [*Wanninkhof*, 1992]. The total flux is similar to Equation D1 and is given as:

$$F_w = k\left([O_2]_{eq} \cdot slpc - [O_2]_{float}\right) \tag{D10}$$

except this time, k is the gas transfer velocity calculated as:

$$k = 0.31 u_{10}\left(\frac{S_c}{660}\right)^{-0.5} \tag{D11}$$

Appendix E: 'Hook' in profiles

Several oxygen profiles from Argo floats have a 'hook' at the deepest 50 m trending towards lower oxygen (Figure E1). At the SCOR Working Group 142 Third Annual Meeting it was proposed that these 'hooks' are either from optode response time or bio/particle fouling, although the cause is still being investigated [*Virginie Thierry,* personal communication]. When calculating our depth-integrated column inventory of oxygen, we integrated oxygen profiles over 0-1900 m to avoid including any 'hooks' at the base of these profiles.

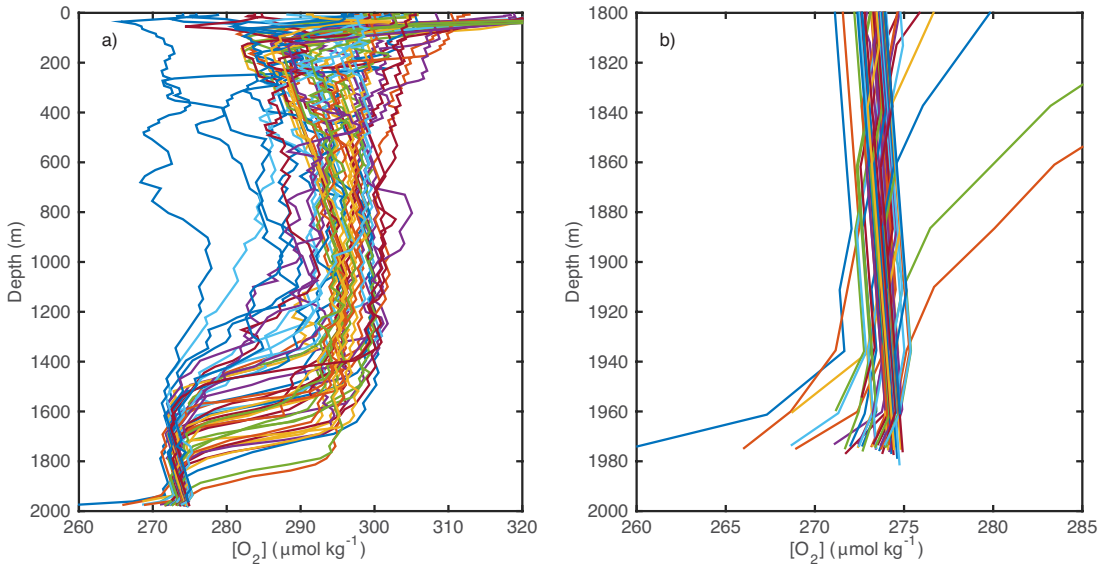

Figure E 1. Oxygen concentration profiles for a) the entire water column and b) the bottom 1800 to 2000 m for float 1901210. The low oxygen 'hook' is visible in the bottom 80 m of some profiles.

Appendix F: Calibration using a reference cast

There are several cases where optodes are calibrated relative to a single deployment profile [e.g. *Kihm and Körtzinger*, 2010; *Koelling et al.*, 2017]. Several issues can arise from this method. First, four of the six optodes used in this study showed drift rates greater than 1.5 μmol kg^{-1} yr^{-1} after deployment. This post-deployment drift would not be accounted for in a calibration method using a single deployment profile. The difference between surface oxygen saturation anomaly from a dataset calibrated using a single deployment profile (ΔO_2^{ref}) and from a dataset calibrated relative to deep ocean values (ΔO_2^{deep}) highlights how a single deployment profile calibration method fails to correct *in situ* optode drift (Figure F1). Furthermore, since Argo floats typically surface only once every 10 days, it can be difficult to obtain ship-based profiles that coincide with both the location and timing of float profiles. This difficulty with finding an initial reference profile adds additional uncertainty. For example, for the four floats in this study exhibiting significant post deployment drift, the closest ship-based profile in time and space was 3 to 70 km away and 2 to 8 days (Figure F1).

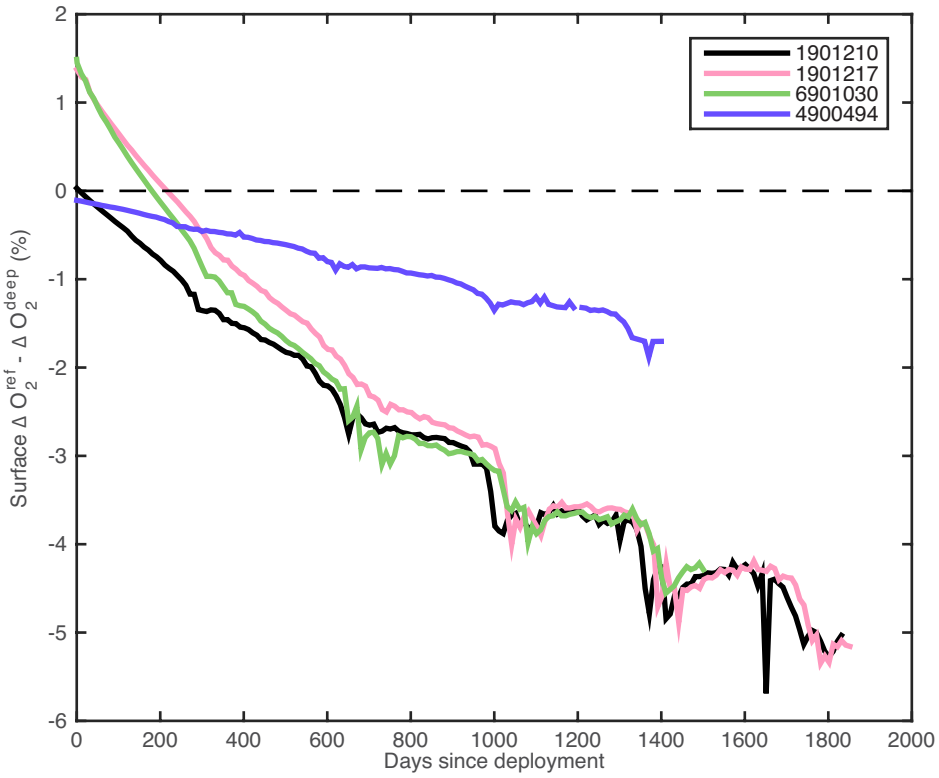

Figure F 1. The difference between surface oxygen saturation anomaly calibrated relative to a single deployment cast (ΔO_2^{ref}) and surface oxygen saturation anomaly calibrated relative to deep-water values (ΔO_2^{deep}) as a function of days since deployment shown for four floats. The closest deployment profile in time and space for each float was: 1.64 days and 7.85 km for float 1901210, 1.92 days and 15.33 km for float 1901217, 1.93 days and 2.29 km for float 6901030, and 8.2 days and 70.21 km for float 4900494.

Appendix G: Oxygen sensor calibration for all floats

All oxygen optodes used in this study needed additional calibration from factory settings. The calibration method used is described in detail in Section 3. It is interesting to note that the three newest floats, 1901210, 1901217, and 6901030, equipped with an Aanderaa optode model 4330 showed significant *in situ* drift that resembled an exponential decay function (Figure G1a, b, and c). Only one of the older floats equipped with Aanderaa optode model 3830, float 4900494, showed significant *in situ* drift that resembled linear decay (Figure G1d) while the other two floats, 4900611 and 4900607, were comparatively stable (Figure G1e and f).

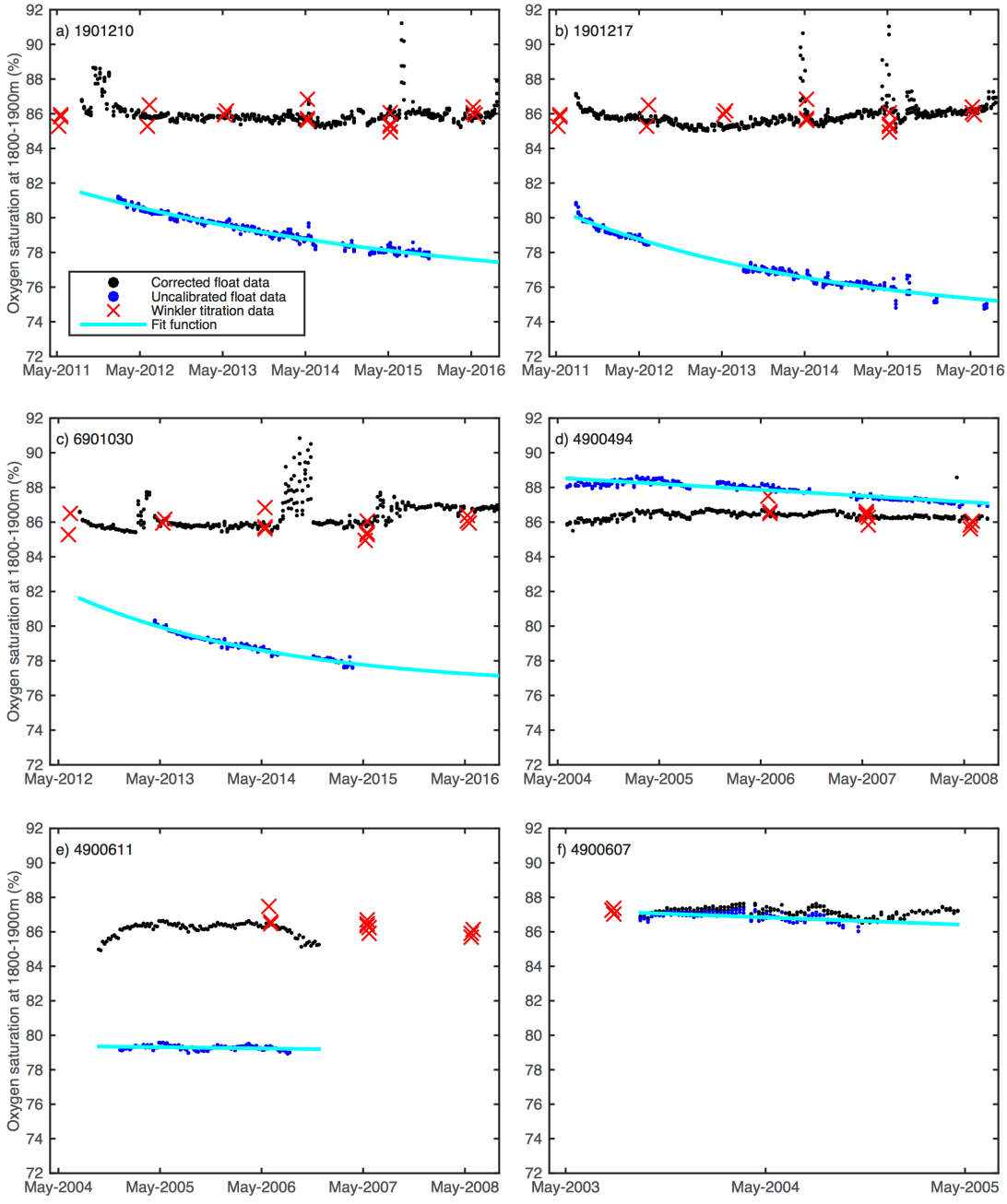

Figure G 1. Corrected oxygen saturation (%) between the depths 1800m to 1900m (black dots) compared to the uncalibrated float data for the same depths used for the fit calculation (blue dots) for all six floats (float number indicated in top left corners). The exponentially decaying fit function (light blue line in a, b, and c) is calculated from Equation 2 while the linearly decaying fit function (light blue line in d, e, and f) is calculated from Equation 3. Winkler titration data at these depths from annual May surveys of the AR7W hydrographic line is shown in red crosses (courtesy of Igor Yashayaev).

Appendix H: Calibration using concentration instead of saturation

We considered calculating and applying the correction gain directly to the measured oxygen concentrations. However, we chose using oxygen saturation as the preferred correction method because optodes measure the partial pressure of oxygen, which is linearly related to the saturation, and the saturation would not respond to temperature driven solubility changes in the way that concentration would [*Takeshita et al.*, 2013]. The absolute difference between surface oxygen saturation anomaly calibrated from concentration (ΔO_2^{conc}) and that calibrated from saturation (ΔO_2^{sat}) is never greater than 0.6 % (Figure H1). The standard deviation of our stable deep-water values is ± 0.7% and therefore the difference between calibrating using concentration and calibrating using saturation falls within our accepted error.

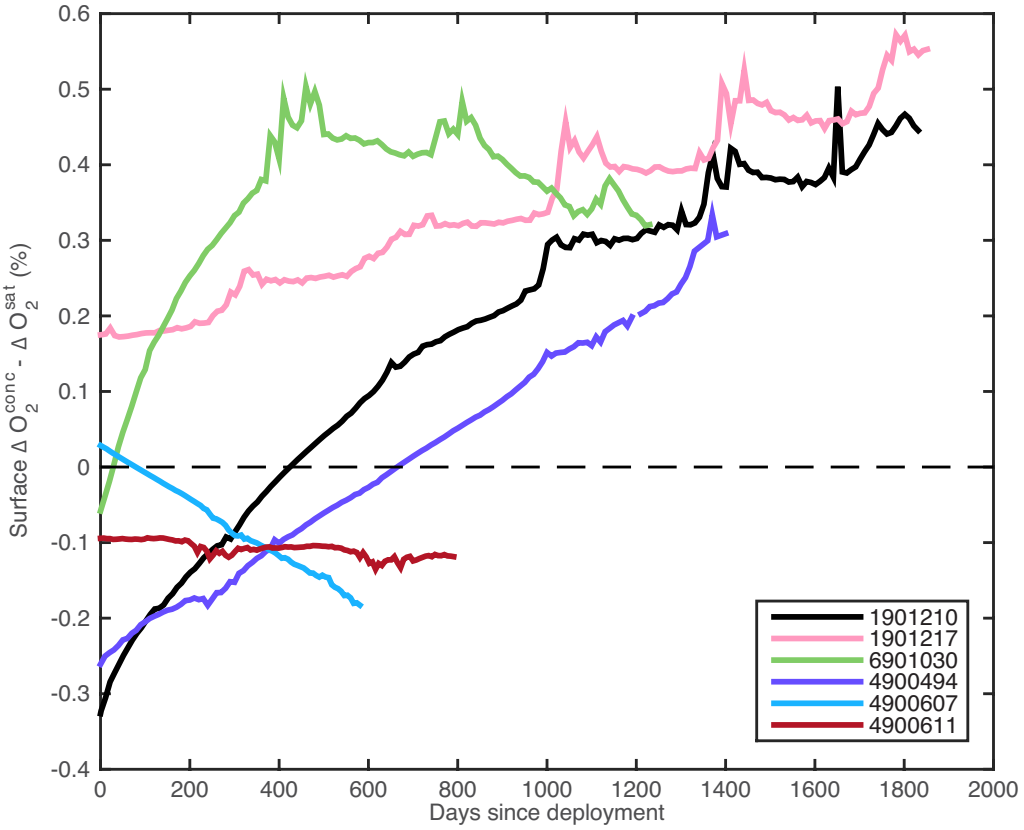

Figure H 1. The difference between surface oxygen saturation anomaly calibrated from concentration (ΔO_2^{conc}) and that calibrated from saturation (ΔO_2^{sat}) for all six floats (float number indicated in legend). This difference is never above ± 0.6 %, within our accepted error of ± 0.7 % based on the standard deviation of our stable deep-water values used in calibration.

Appendix I: Float 4900494 in-air calibration method versus this study

Johnson et al. [2015] calibrated float 4900494 using an in-air calibration method. The mean surface ΔO_2 difference between the *Johnson et al*. [2015] calibration and our method for float 4900494 was 0.49 ± 0.36 %, with the standard deviation arising from the drift during deployment that our method corrects (Figure I1). The in-air oxygen calibration method is capable of producing a time-dependant gain to correct for drift [*Bushinsky et al.,* 2016], however the *Johnson et al*. [2015] calibration does not correct for post-deployment drift.

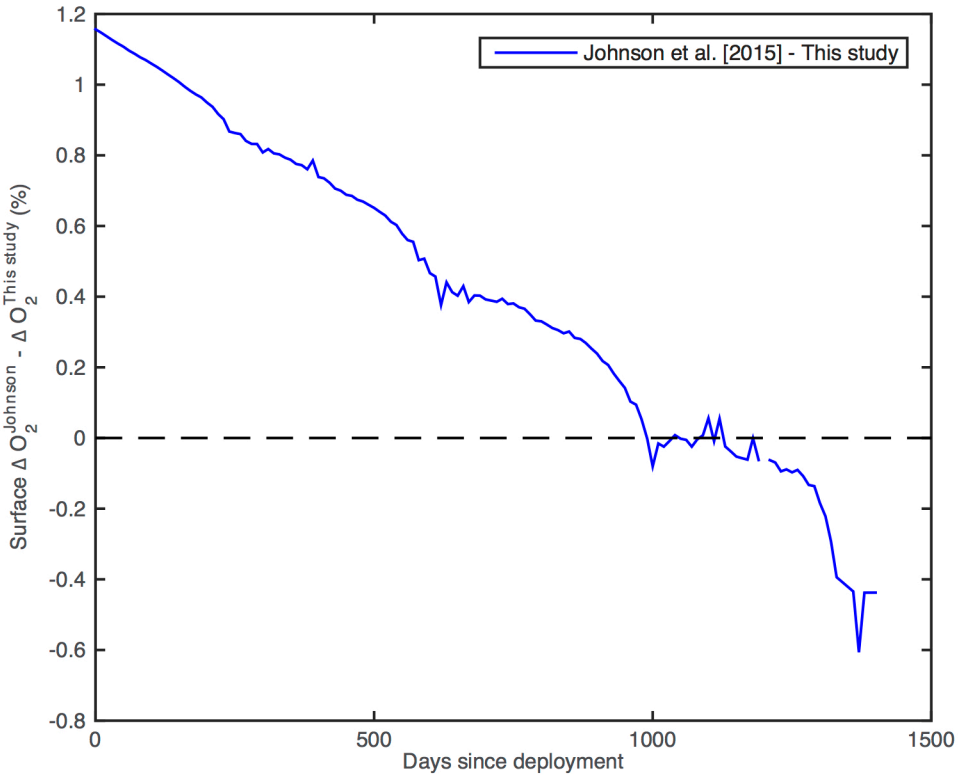

Figure I 1. The difference between float 4900494 surface ΔO_2 (%) calibrated using in-air measurements from *Johnson et al.* [2015] and surface ΔO_2 (%) calibrated using the method from this study, as a function of days since deployment.

Appendix J: Surface heat fluxes as a predictive variable

Surface heat fluxes as a potential predictive variable did not have as strong a correlation to the end of convection oxygen saturation anomaly as the maximum depth of convection and the end date of convection (Figure J1). Wintertime convection in the Labrador Sea depends on both the atmospheric forcing and the preconditioning of the water column. Surface heat flux does not capture the preconditioning of the water column, while maximum depth of convection and end date of convection capture both preconditioning and atmospheric forcing.

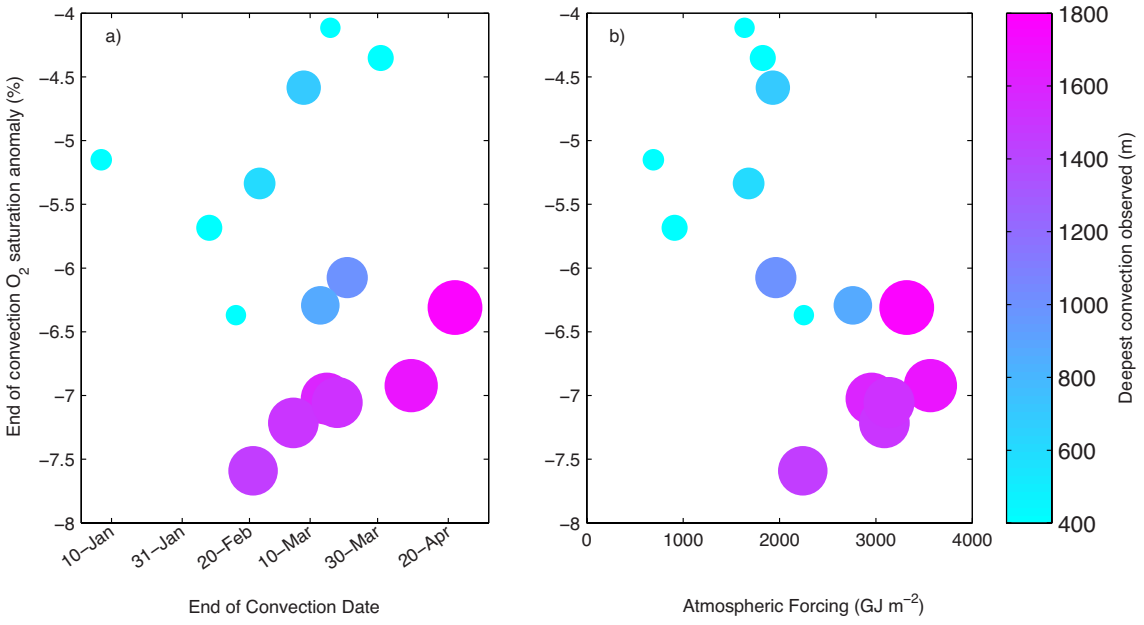

Figure J 1. The end of convection surface oxygen saturation anomaly (%) as a function of a) convection end date and b) as a function of atmospheric forcing (GJ m^{-2}). The colour and size of the dot represents the maximum depth of convection observed by the float (bigger and more pink is deeper, smaller and more blue is shallower).

Appendix K: Cumulative fluxes versus column-integrated inventory

The cumulative fluxes from both the *Liang et al.* [2013] and the *Wanninkhof* [1992] parameterization are compared to the depth-integrated column oxygen inventory for all six floats used in this study (Figure K1), as opposed to just four floats shown in Figure 7 in the paper.

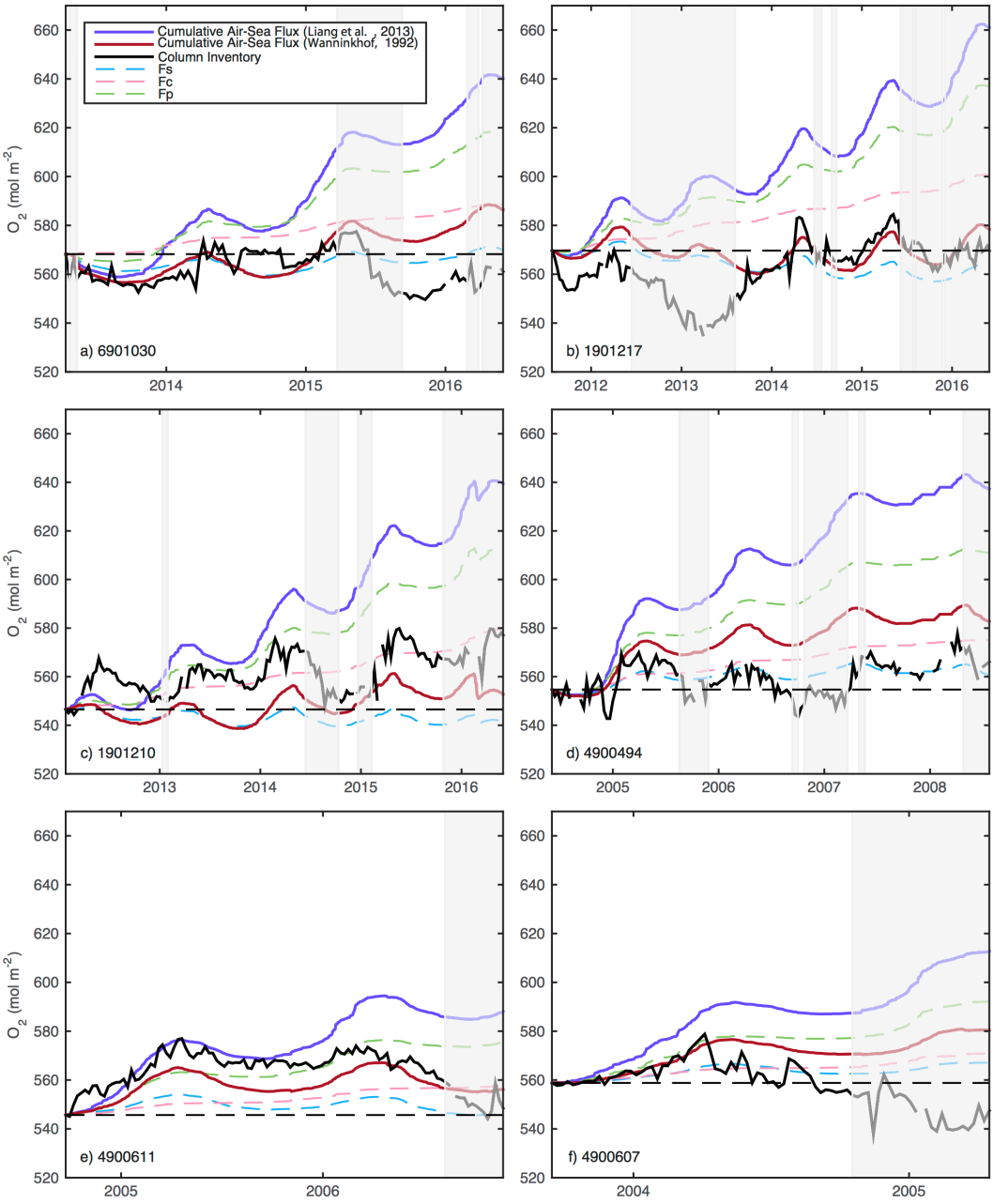

Figure K 1 Time series of the cumulative air-sea flux (mol m^{-2}) calculated using the *Liang et al.* [2013] gas exchange parameterization (solid purple line) and the *Wanninkhof* [1992] parameterization (solid dark red line) compared to the oxygen column inventory from 0 to 1900 m (solid black line) for all six floats (float number indicated in lower left corners). The three individual flux components of *Liang et al.* [2013] are also shown: the air-sea interface (F_S, dashed blue line), completely dissolving bubbles (F_C, dashed pink line), and partially dissolved bubbles (F_P, dashed green line). The grey shaded regions represent time periods when the float left the study region (Figure 1).

Appendix L: Lateral mixing end members

Defining the outside endmember for quantifying the lateral flux of low oxygen water into the Labrador Sea creates significant uncertainty in this analysis. We used profile data from two floats (1901210 and 6901030) while they spent time in the Irminger Sea (Figure L1) and a combination of T/S, T/O_2, and S/O_2 plots (Figure L2), as well as depth profiles of each property, to isolate Icelandic Slope Water (ISW), Irminger Current (IC), and Irminger Sea water (IS). We chose three different mixing ratios to calculate our outside endmember, representing a lateral flux composed of 100% boundary water (IC), 100% interior water (IS), and a mix between the two with ISW also contributing to the boundary water (25% IS, 25% IC, 50% ISW). The cumulative combination of the lateral flux based on these three ratios and air-sea gas exchange can closely represent the observed balanced oxygen inventory (Figure L3).

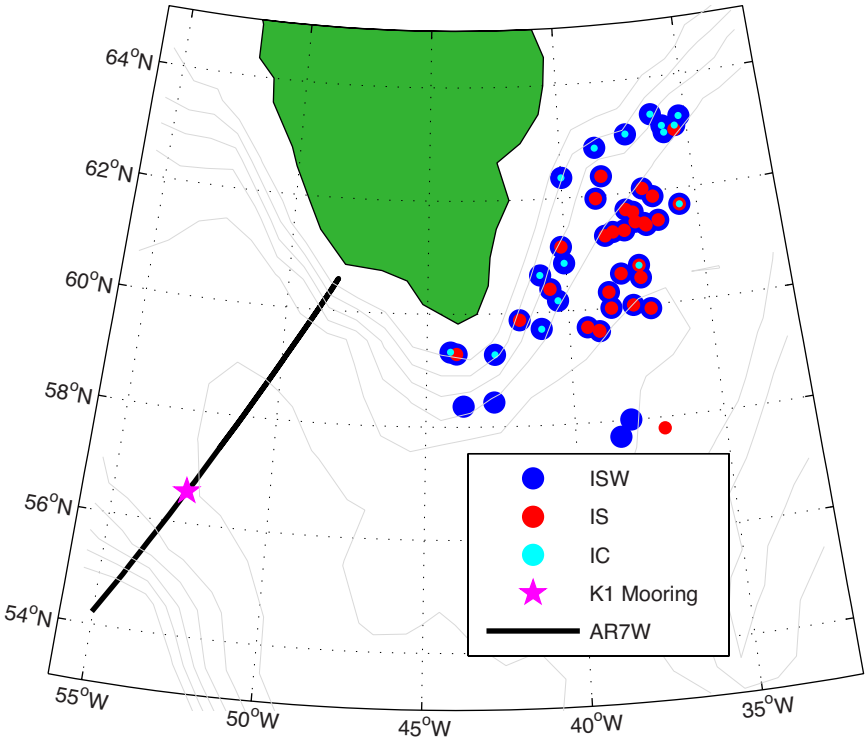

Figure L 1. Map of profile locations in the Irminger Sea from floats 1901210 and 6901030. The size of the dot represents the average depth of the water mass, with Icelandic Slope Water (ISW, blue circles) at 1270m ± 83 m, Irminger Sea water (IS, red circles) at 742 ± 28 m, and Irminger Current water (IC, cyan circles) at 290 ± 58 m. Also shown is the location of the K1 mooring site (purple star) and the AR7W hydrographic line by Fisheries and Oceans Canada (black line). Grey lines indicate bathymetry at 500 m intervals, starting at 1000 m.

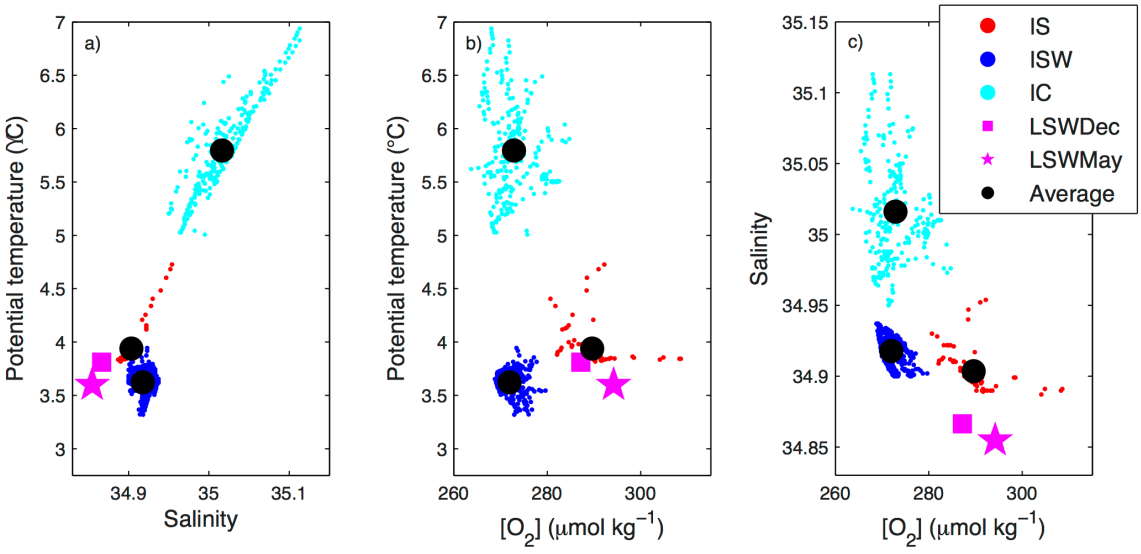

Figure L 2. a) Potential temperature (°C) versus salinity, b) potential temperature versus dissolved oxygen (µmol kg^{-1}), and c) salinity versus dissolved oxygen highlighting the three water masses used as outside endmembers for the lateral flux analysis. The Irminger Sea water (IS, red circles), Icelandic Slope Water (ISW, blue circles), and the Irminger Current (IC, cyan circles) have average end member properties marked by black circles. The purple star and purple square denotes the endmember for the Labrador Sea in May (LSWMay) and December (LSWDec) respectively.

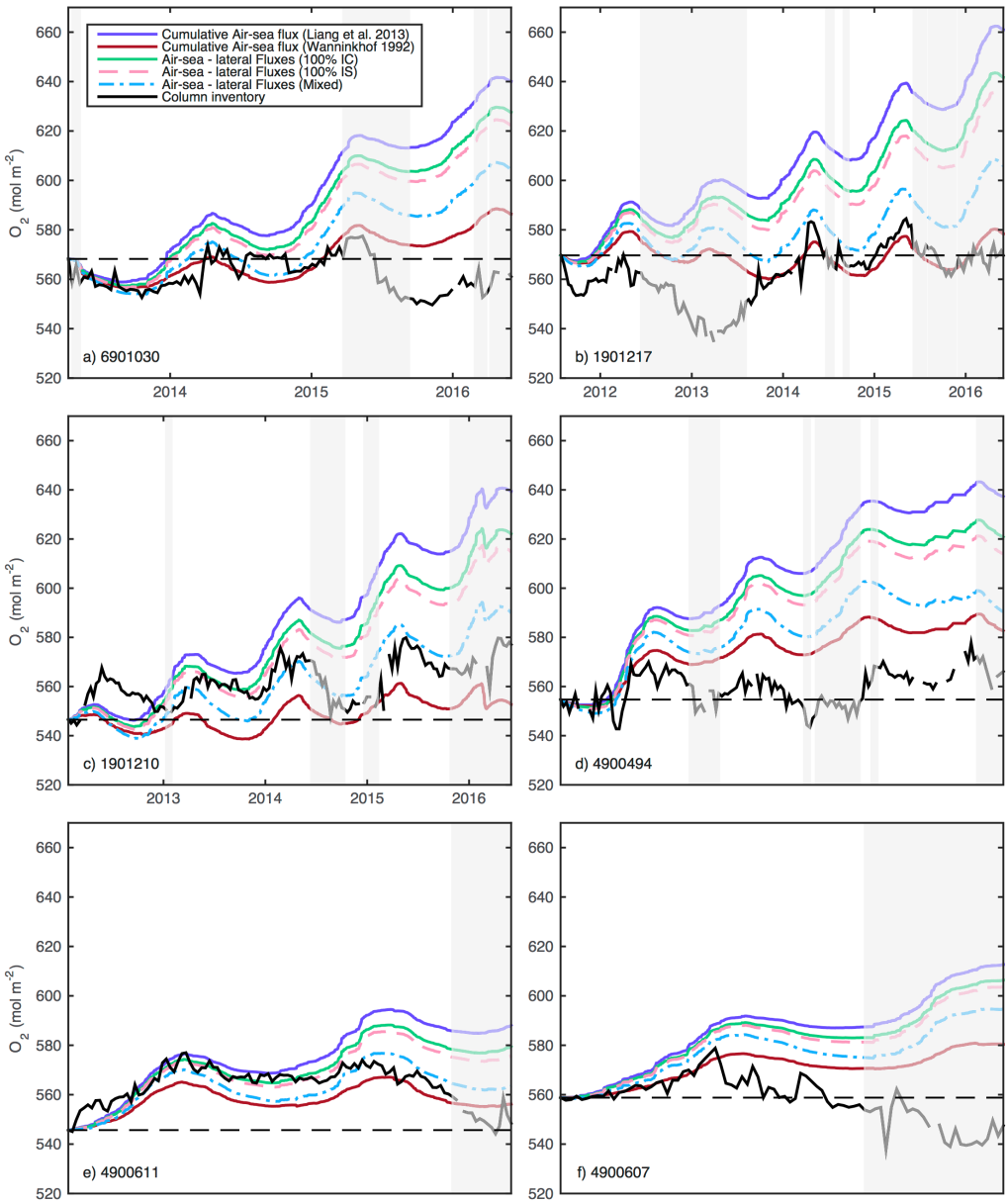

Figure L 3. Time series of the cumulative air-sea flux (mol m^{-2}) calculated using the *Liang et al.* [2013] gas exchange parameterization (solid purple line) and the *Wanninkhof* [1992] parameterization (solid dark red line) compared to the oxygen column inventory from 0 to 1900 m (solid black line) for all six floats (float number indicated in lower left corners). The cumulative combination of the lateral flux from three endmember mixing ratios and the air-sea flux of *Liang et al.* [2013] are also shown: 100% IC endmember (solid green line), 100% IS endmember (dashed pink line), and mixed (25% IS, 25% IC 50% ISW) endmember (dashed blue line). The grey shaded regions represent time periods when the float left the study region (Figure 1).